17

Modeling and Simulation of Microscale Flows

Auro Ashish Saha and Sushanta K. Mitra[1]
Department of Mechanical Engineering, Indian Institute of Technology Bombay, Mumbai India

Abstract

Modeling and simulation are very powerful tools and have become an integral part in the design and development of engineering systems. In the microscale domain, modeling and simulation have been applied in the development of microfluidic devices. Microdevices developed for sample mixing, sample dispersion, drug discovery, biochemical analysis and micropower systems have become possible only due to the impetus and insight gained from the simulation studies of fundamental microfluidic problems. Microfluidic device modeling comprises of dealing with interplay of multiphysics phenomena such as fluid flow, structure, surface and interfaces, etc. As the surface area to volume ratio increases with the decrease of the system feature size of microdevices, some physical phenomena which are insignificant in the macro domain become prominent in the micro domain. Some of the tried and tested macroscale theory and experimental results no longer show similar trends in the microscale. Hence dealing with simultaneously widely differing physics becomes too complicated in the microscale which include microfluidics, microtransport, microthermal, micromechanics, microlectronics and optics with biochemical thermodynamics and reaction kinetics. In this article, the use of numerical modeling and simulation techniques for flow in microchannels applied to microfluidic devices are presented encompassing all the relevant physics at the microscale by the state of the art multiphysics simulation tools such as CFD-ACE+, COMSOL, Fluent to name a few. Numerical simulation of electroosmotic effect on pressure-driven flows in the serpentine channel of a microfuel cell with variable zeta potential on the side walls is investigated and reported. The Poisson-Boltzmann and Navier-Stokes equations are solved numerically to investigate the electroosmotic driven flow phenomena. It is observed that vortices are developed at the straight portion of the microchannel due to the electroosmosis. Flow control in the serpentine microchannel by regulating the zeta potential at the bend has also been demonstrated. Capillary driven flow in a microchannel with alternate hydrophilic-hydrophobic patterns on the bottom wall is investigated for bioreactor applications. The transient flow is modeled by coupling the incompressible Navier-Stokes equation with the interface evolution equation using volume of fluid (VOF) methodology. Higher order surface reconstruction method is adopted for interface tracking. Flow instability increases as the fluid traverses alternately between the hydrophilic and hydrophobic regions. Such flow phenomena in the microchannel indicate that flow control is possible by patterning the channel walls for applications related to

[1] Corresponding Author; Email: skmitra@iitb.ac.in

microfluidic devices. The simulation of dynamic interaction between an elastic membrane structure and fluid in a two-dimensional microchannel is also reported here. The viscous and pressure forces imposed by the fluid flow cause the deformation of elastic membrane which significantly affects the flow field. This involves formulating a coupled fluid structure interaction (FSI) model for the demonstrated case. The solution schemes used for this analysis are based on Lagrangian formulations for the structural parts and Arbitrary Lagrangian Eulerian (ALE) formulations for the fluid regions.

Keywords: Modeling, microchannel, transport, simulation, electroosmotic flow, free surface flow, fluid structure interaction

Nomenclature

Bo	Bond number
Ca	Capillary number
C_0	Ionic concentration in bulk solution
D_h	Hydraulic diameter of channel cross section
d	Diameter of circular top
E	Electric field intensity, elasticity of structure
F	Faraday's constant, liquid volume fraction
F_s	Volumetric force representing the surface tension
H_c	Channel depth
h	Local cell dimension
L	Half length of section of straight segment of channel, channel length
l	Height of structure
n	Normal vector
$\hat{n}$	Unit vector normal to the surface
$\hat{n}_w$	Unit vector normal to the wall
P	Pressure
p	Pressure
Re	Reynolds number
R_c	Radius of curvature of channel axis at U-bend
R_u	Universal gas constant
t	Time
$\hat{t}_w$	Unit vector tangent to the wall
U	Characteristic velocity
u	Velocity component in x-direction
u_{in}	Inlet velocity
V	Velocity vector
V_{inlet}	Velocity of fluid at inlet
v	Velocity component in y-direction, interface velocity
W	Channel height
W_c	Channel width
w	Velocity component in z-direction, width of base structure
z_e	Valance number of univalent fluid
$z_{+/-}$	Valance number of the positive/negative ions in the fluid

Greek symbols

ϵ	Permittivity of fluid
λ	Debye length
μ	Viscosity of fluid
ϕ	Applied potential
ψ	Potential due to electrical double layer
ζ_w	Zeta potential or wall potential
ρ	Density of fluid
ρ_E	Charge density
σ	Surface tension of fluid
θ	Contact angle
η	Viscosity of fluid
κ	Curvature of the surface

Subscripts

c	Channel
in	Inlet
s	Surface tension
w	Wall

1. Introduction

Microfluidics refers to devices and methods for controlling and manipulating fluid flows with length scales less than a millimeter. Microfluidic flows are readily manipulated using many kinds of external fields (pressure, electric, magnetic, capillary, etc.). Microfluidic systems have revolutionized by automation of chemistry and biology, by enabling possibility of numerous experiments performed rapidly and in parallel, while consuming little reagent. A large surface-to-volume ratio is a common characteristic for microfluidics architecture so that, relative importance of surface to volume forces increases. A large surface-to-volume ratio results in the dominance of the viscous effect over the momentum effect. Microfluidic flow is usually a low Reynolds number flow. Fluid/surface interactions become more significant as the dimensions shrinks resulting in a very large surface-tension-driven pressure difference. Flow control is essential in many of the microfluidic systems targeted for use in biochemistry analysis, drug delivery, and sequencing or synthesis of nucleic acids, among others. Such systems use microchannels to promote efficient mixing without the use of any external means. These devices typically rely upon the balance of surface tension and fluid pressure forces to perform their function.

The use of numerical simulation and computational techniques applied to the design and development of microfluidic devices is reviewed here. The transport of pressure-driven, electroosmotic, capillary-driven and flows with fluid structure interaction in microchannels are presented. As microfluidic devices become increasingly complex, it is difficult to perform reliable experiments and hence one needs to rely on numerical tools for optimal fluidic and transport designs. There are a variety of commercially available numerical softwares that have been successfully used in modeling microfluidic devices (eg., COMSOL, CFD-ACE+, Fluent and Coventor). These tools offer multiphysics capabilities which

facilitate the coupling and simultaneous solution of different fundamental equations governing the physics of a given problem.

2. Electrokinetic Flows in Microchannels

Electroosmosis is the motion of fluid caused by externally applied electric potential. In practice, most surfaces contain a residual negative charge. When such charged surface comes in contact with ionizing fluid, the ions having polarity opposite to the surface charge are attracted towards the surface. These ions accumulate near the surface, forming an *electric double layer (EDL)*. In this layer ion concentration changes from a maximum value (zeta potential, ζ_w) near the wall to a neutral state in the fluid core. The thickness of this layer is characterized by Debye length, λ, which is defined as the distance from the solid surface to which the charge drops to e^{-1} (37%) of its maximum value. The typical range of zeta potential and Debye length is $20 - 150\ mV$ and $10^{-9} - 10^{-6}$ m, respectively (Brant et al., 2005; Liechty et al., 2005). When electric potential is applied across a capillary, the ions in the EDL move under the influence of the electric field. This ion movement causes bulk fluid motion due to the momentum transfer from EDL to the fluid core.

The convective transport in micro domain is of great importance as it applies to various application such as Micro Electro Mechanical Systems (MEMS) devices, micro-heat exchangers, micro-fuel cells, etc. (Rawool et al., 2006). In fuel cells, the typical fuel such as hydrogen for Proton Exchange Membrane (PEM) or methanol for Direct Methanol Fuel Cell (DMFC), flows through the serpentine flow field present in the bi-polar plates of the cell. Due to the electric potential generated in the micro-fuel cell, a potential gradient is developed in the bi-polar plate, the direction of which is perpendicular to the flow direction. The presence of an aqueous solution in the flow field such as methanol in case of DMFC, results in electroosmosis driven flow, which is of interest for micro-fuel cell applications.

There have been a few studies reported in the field of electroosmosis driven flow in micro DMFC. Karimi and Li (2005) have modeled the electroosmotic flow in the fuel cell membrane including the electrokinetic effect. They have modeled the membrane pore to determine the electroosmotic flow through the membrane for different geometrical and operating conditions. They have reported a nonlinear increase in electroosmotic flow with increase in pore size and found that the electroosmotic drag coefficient increases linearly with pore size.

Several researchers have investigated the effect of varying zeta potential on electroosmotic flow (EOF) in microchannels (Fu et al., 2003; Herr et al., 2000; Chen et al., 2006; Lee et al., 2005; Zhang et al., 2006). Such EOF are in the direction of the pressure driven flow. The characteristics of EOF in a microchannel depend upon the nature of the zeta potential, i.e., whether it is uniform or nonuniform. Fu et al. (2003) used Nernst-Planck equation along with a Navier-Stokes solution to model the EOF that occurs when a step change in zeta potential is applied. The results indicate that a step change in zeta potential causes a significant variation in the velocity profile and also in the pressure distribution.

Microscale debris and manufacturing irregularities during fabrication of microchannels, and adsorption of organics during analysis of microchannels produce nonuniform zeta potential distributions along the channel walls. Herr et al. (2000) have shown the influence of zeta potential on the velocity profile and sample dispersion rate for electroosmotic flow in cylindrical capillaries with nonuniform zeta potential distribution. Similarly, Chen et al.

(2006) investigated numerically the effects of step change in zeta potential in a cylindrical microchannel on electroosmotic flow. It is observed that the variable zeta potential along the flow direction generated regions of positive and negative pressure gradients in the flow field. Lee et al. (2005) studied electroosmotic flow in a cylindrical microchannel with non-uniform zeta potential distribution. They showed formation of distorted electroosmotic velocity profiles and flow circulation resulting from the axial variation of the zeta potential. However, these studies are related to straight microchannels only.

Zhang et al. (2006) studied the two dimensional flow pattern in microchannels with large aspect ratios with heterogeneous zeta potentials, and discuss the formation of secondary EOF's generated by wavelike zeta potential. Their results show that the heterogeneous zeta potentials could generate complex flow patterns and enhance mixing. However, their study may not be representative for microchannels with nearly square cross section.

Souders et al. (2003) have studied combined electroosmotic and pressure driven flows in a three dimensional microchannel with walls covered by charged bands. Under the influence of electroosmotic flow only, it is found that there is a significant amount of fluid folding and stretching. By adding pressure gradient against electroosmotic flow, they showed an increase in the fluid particle residence time. The helical flow structure is also observed for this combined electroosmotic and pressure driven flow.

Fuel feed into the micro fuel cell is an important process affecting its power density and often there is a need to minimize power loss accounting from fuel delivery. Buie et al. (2006) presented a novel design and performance of a planar silicon electroosmotic pump (EO) for methanol fuel delivery in DMFC. Though the EO pump could not deliver enough pressure head for fuel delivery, nevertheless it was interesting to note that the micro DMFC has shown to have improved polarization and power density characteristics with the EO pump. The study in particular emphasizes the performance enhancement due the combined mechanism of electroosmotic phenomena and diffusion for fuel delivery.

Rawool and Mitra (2006) studied the transport of methanol in micro-fuel cell under the applied potential which is perpendicular to the direction of the flow with the side walls of the channels subjected to a constant zeta potential. As observed in the existing literature (Herr et al., 2000; Chen et al., 2006) the zeta potential tend to change along the flow field as the fuel gets consumed in the chemical reaction occurring at the catalyst layer, adjoining the flow channels. The heterogeneous zeta potentials in microchannels can also be achieved through chemical modifications, coupled capillaries and integrated systems (Zhang et al., 2006). Hence, Saha et al. (2007) performed numerical studies to understand the flow behavior in the microchannel of the fuel cell under variable zeta potential conditions.

2.1 Governing Equations

The force acting on ions is accommodated as a body force in Navier-Stokes equation, which reads as

$$\rho(V.\nabla)V = -\nabla P + \mu\nabla^2 V + \rho_E E \tag{1}$$

where ρ_E is the charge density and E is the electric field. For steady flow with constant properties, the continuity equation can be written as

$$\nabla.V = 0 \tag{2}$$

The electric field E in Eqn. (l) has two contributions. One is the field due to applied potential (ϕ) for which governing equation is

$$\nabla^2 \phi = 0 \tag{3}$$

The second contribution is the field due to EDL which is governed by the equation

$$\nabla^2 \psi = -\frac{\rho_E}{\epsilon} \tag{4}$$

The charge density is given by

$$\rho_E = FC_0 z_- e^{(z_- F\psi/R_u T)} - FC_0 z_+ e^{(z_+ F\psi/R_u T)} \tag{5}$$

which, for a symmetric electrolyte of valance number z_e becomes

$$\rho_E = 2FC_0 \sinh\left(\frac{z_e F\psi}{R_u T}\right) \tag{6}$$

where ψ is the potential due to electrical double layer, F is Faraday's constant, R_u is universal gas constant. The Poisson-Boltzmann and Navier-Stokes equations are solved numerically to investigate the electroosmotic driven flow phenomena for prescribed operating conditions.

2.2 Numerical Simulation

Physical Problem

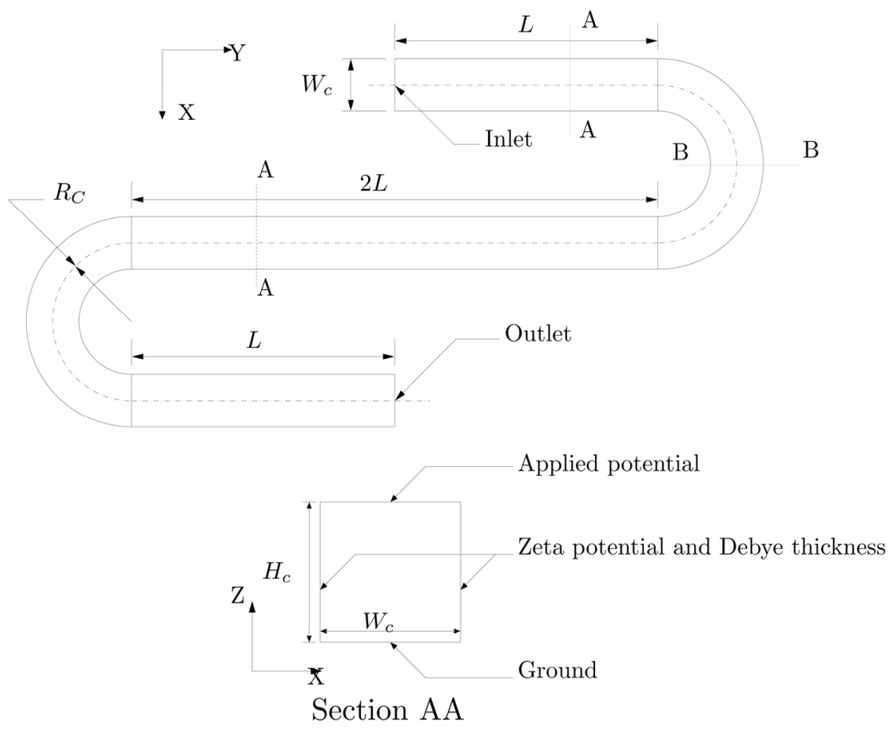

Figure 1. Geometry of serpentine channel

In Fig. 1 schematic of the serpentine microchannel model is shown. The channel considered here is a three dimensional serpentine channel. The cross sectional area of the channel is 100 μm x 100 μm. The model consists of a single 'S' shaped segment of the serpentine channel. It has three straight lengths connected by two semicircular arcs. In Fig. 1 length L = 300 μm and the radius of curvature at bend is R_c = 200 μm.

Boundary Conditions

For fluid flow, a constant velocity corresponding to a given Reynolds number is specified at the channel inlet. At outlet, a constant pressure (atmospheric) is specified. No slip boundary condition is imposed on all the remaining walls. Following is the mathematical representation of the above conditions:

$$\left.\begin{array}{l} u = 0 \\ v = Const. \\ w = 0 \end{array}\right\} \quad \text{for} \quad \left\{\begin{array}{l} 0 < x < 100\ \mu m \\ y = 0 \\ 0 < z < 100\ \mu m \end{array}\right.$$

$$P = 0 \quad \text{for} \quad \left\{\begin{array}{l} 4R_c\ \mu m < x < 4R_c + 100\ \mu m \\ y = 0\ \mu m \\ 0 < z < 100\ \mu m \end{array}\right.$$

$$\left.\begin{array}{l} u = 0 \\ v = 0 \\ w = 0 \end{array}\right\} \quad \text{for all other boundaries}$$

For electric field, a fixed potential is specified at top and bottom walls of the channel, as shown in Fig. 1, which can be expressed as,

$$\phi = 0 \quad \text{Volt} \quad \text{for} \quad \left\{\begin{array}{l} z = 0 \\ \text{for all x and y} \end{array}\right.$$

$$\phi = 0.1 \quad \text{Volt} \quad \text{for} \quad \left\{\begin{array}{l} z = 100\ \mu m \\ \text{for all x and y} \end{array}\right.$$

A zeta potential and Debye length are specified on the side walls of the channel as shown in Fig. 1. The Debye length is kept constant at 1 x 10^{-7} m. The zeta potential is varied linearly on both walls, to investigate the effect of zeta potential profile on the electroosmotic flow. The variable zeta potential condition can be expressed mathematically in the following manner:

$$\left.\zeta_w = -0.01 - \frac{(0.09 - 0.01)}{(100 \times 10^{-6})} ZV \quad \text{for} \quad 0 < z < 100\ \mu m \right\} \text{On the left and right wal1}$$

Numerical Technique

The channel geometry is created and meshed using CFD-GEOM modeler. Structured grid is used for simulations. A grid independence study is carried out by successively refining the grid, increasing the number of elements in the domain. The grid is made extra fine in the near wall region where maximum gradients occur. For a grid having 260431 elements, the solution is found to be grid independent. Hence this mesh size was used in all the cases.

CFD software CFD-ACE+ is used for the simulations. Upwind scheme is used in the CGS+Pre solver (ESI CFD Inc., 2006) for velocity and electric field while AMG solver is used for pressure correction. Parametric solver is used to solve for values of inlet velocity corresponding to a range of Reynolds number. A Reynolds number of 0.001 is used in the simulations. Here, Reynolds number is defined as

$$Re = \frac{\rho V_{inlet} D_h}{\mu}$$

where D_h is the hydraulic diameter of the channel, defined as

$$D_h = \frac{4(W_c \times H_c)}{2(W_c + H_c)}$$

Here W_c is the width of the channel and H_c is the depth of the channel as shown in Fig. 1. The effect of zeta potential profile on the velocity profile in the channel is studied. The physical and dielectric properties of methanol at 25° *C* used for simulations are provided in Table 1.

Physical property	Value	Dielectric property	Value
Density *(kg/m³)*	785	Electric conductivity (1/ohm-m)	4.4 x 10^{-4}
Viscosity *(Pa. s)*	5.6 x10^{-4}	Relative permittivity	33.62

Table 1. Properties of methanol

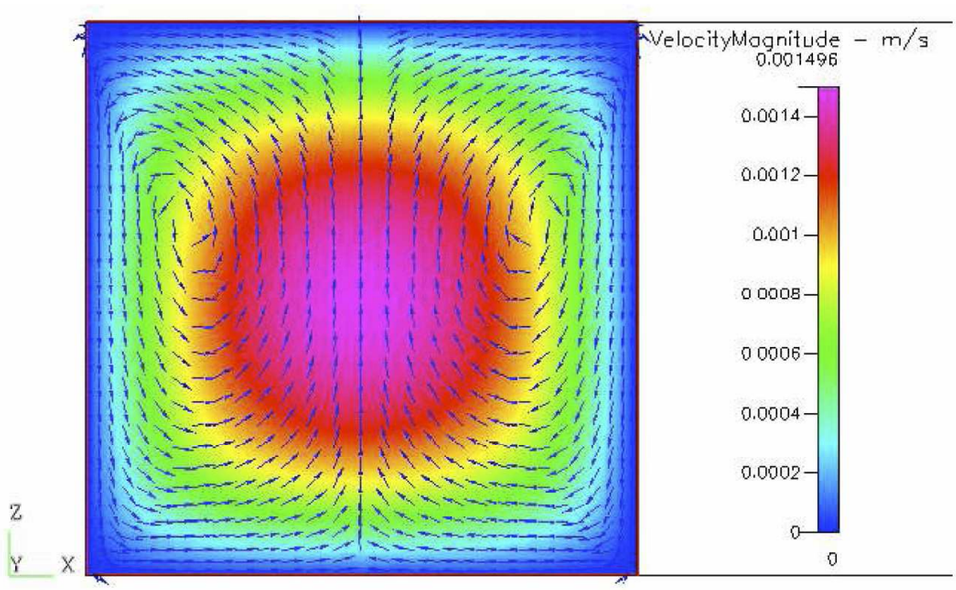

Figure 2. Flow pattern in the channel cross section at 150 μm from channel inlet (section AA in Fig. 1)

Results and Discussion

The velocity vectors in the straight portion of the microchannel, at a distance of 150 μm from the channel inlet, is shown in Fig. 2. The color indicates the velocity magnitude $\sqrt{u^2+v^2+w^2}$ while the vectors indicate direction of in-plane component $\sqrt{u^2+w^2}$. It can be

seen that due to electroosmotic driving force, a secondary vortex pair has been generated in the flow cross section such that the fluid near the side walls moves towards the bottom plate. The fluid again rises in the central portion of the channel to maintain the continuity. Thus two distinct vortices are formed due to electroosmosis. These kind of vortices are absent in case of flow without electroosmosis. This modified flow profile gives rise to additional pressure drop in case of flow with electroosmosis (Rawool & Mitra, 2006). The centers of both the secondary vortices are shifted towards the top wall due to gradual change in the electroosmotic driven force on the fluid as the zeta potential is linearly varied for each wall. This results in shifting of the secondary vortex by a smaller distance. The streamline plot is shown in Fig. 3 which depicts the formation of vortices and the effect of variable zeta potential is clearly seen.

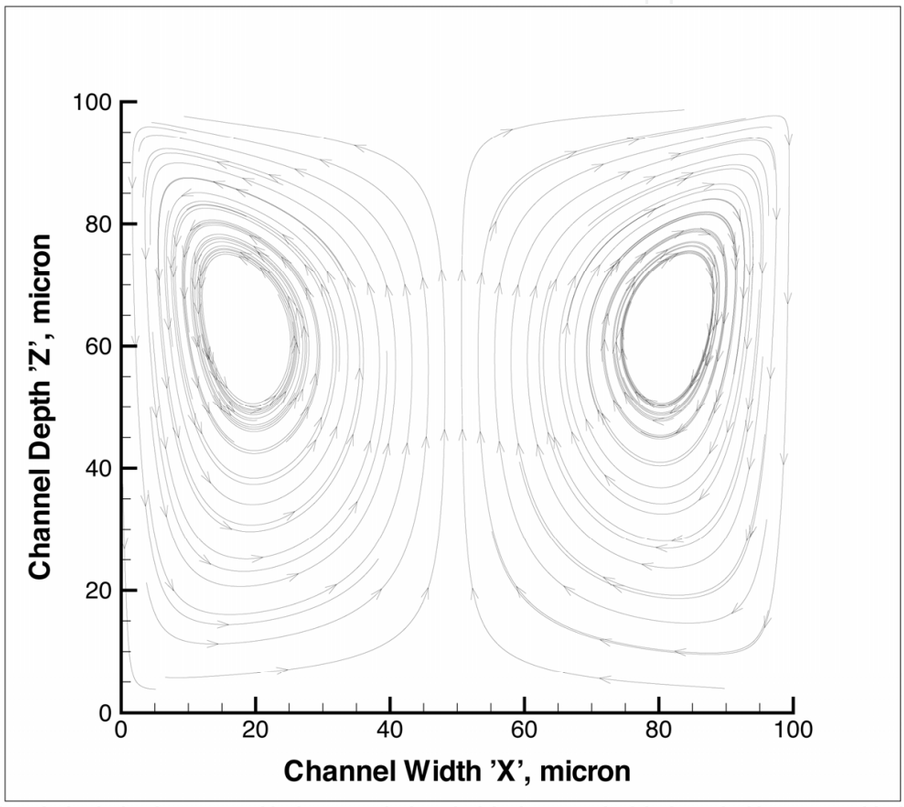

Figure 3. Streamline plot in the channel cross section at 150 μm from channel inlet (section AA in Fig. 1)

The flow behavior at the semi-circular bend for section BB in Fig. 1 has also been studied for four different cases. Figure 4 shows the streamline plots at the bend for pressure driven flow and the applied zeta potential of -0.1 mV, -1 mV and -50 mV, respectively. Fig. 4a shows the formation of vortices purely due to the pressure-driven flow with no contribution from the electroosmotic effect. As the applied zeta potential is increased at the semi-circular bend (section BB in Fig. 1), the electroosmotic forces cause the vortices to shift in a clockwise direction as shown in Fig. 4d. The observed shift of secondary vortices in a clockwise direction with an increase in the applied zeta potential presents an excellent opportunity for obtaining flow control in the serpentine microchannel by regulating the zeta potential at the

bend. Formation of additional vortices at the top left and bottom right corners has also been observed when the applied zeta potential is -0.1 mV, as shown in Fig. 4b.

Figure 5 shows the z component of velocity along the channel width at z = 50 μm for the cross section BB. It is observed here that for a pressure-driven flow only, the z component velocity is zero as the secondary vortices appear at the center line and results in a zero velocity at the central core. It is found that the z component reaches a maximum at a small distance from the wall when zeta potential of -0.1 mV, -1 mV and -50 mV is applied on the side walls. The maximum velocity is reached for the -50 mV of applied zeta potential and decreases in magnitude as the applied zeta potential is reduced. The velocity component then drops to zero and again reaches a maximum value in opposite direction at the center of the channel. Hence, it can be concluded that the z component velocity influences the formation of vortices in the semi-circular bend at the cross section BB and results in the shifting of the vortices in the clockwise direction.

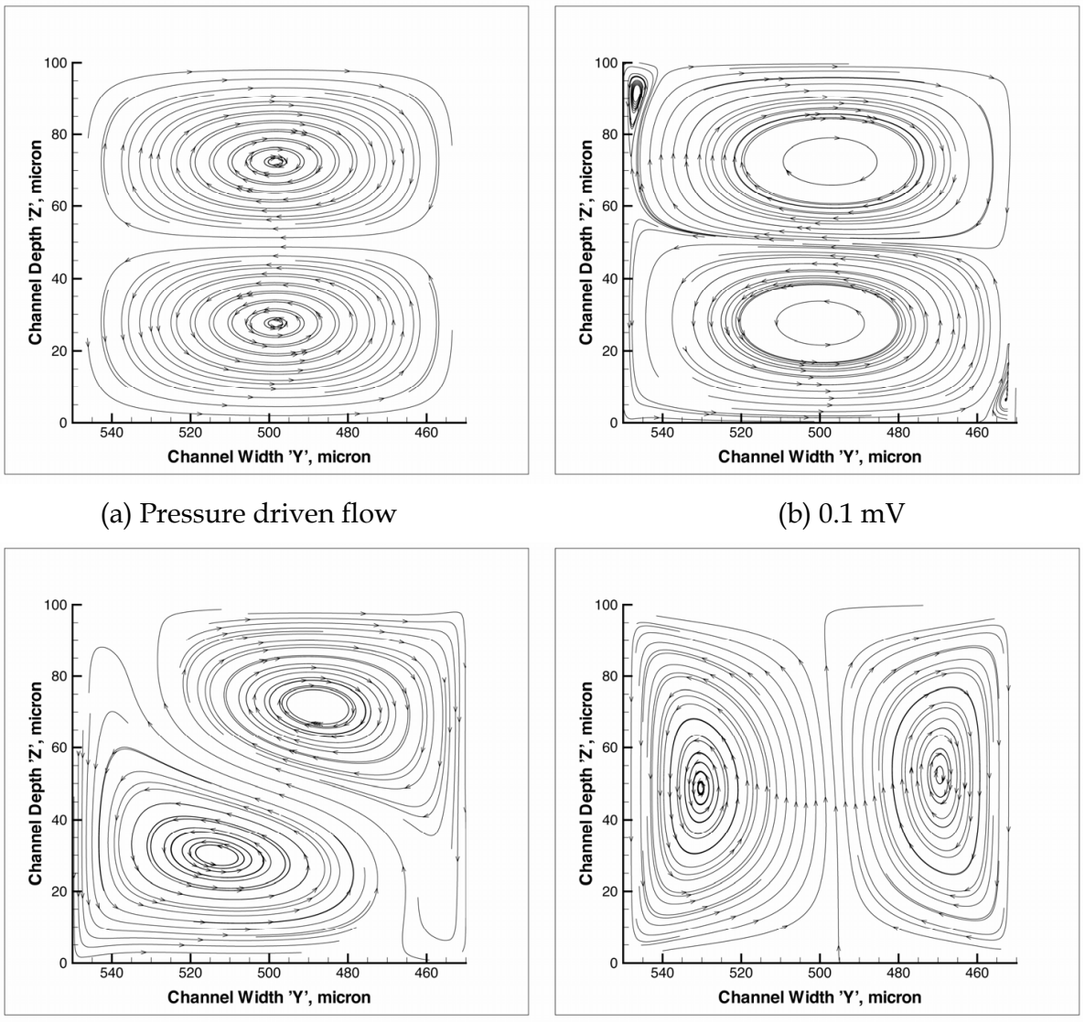

(a) Pressure driven flow (b) 0.1 mV

(c) 1 mV (d) 50 mV

Figure 4. Streamline plots in the channel cross section at the bend (section BB in Fig. 1) for different zeta potential values

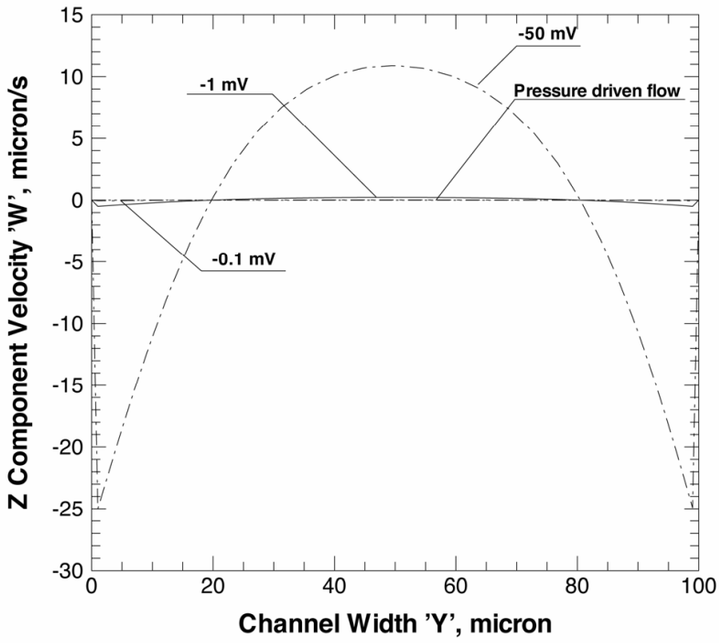

Figure 5. Variation of z component of velocity at z = 50 μm along the channel width at section BB

3. Free Surface Flows in Microchannels

An interface between a gas and liquid is often referred to as a free surface. There are large differences in the densities of the gas and liquid at the interface. The only influence of the gas is the pressure it exerts on the liquid surface and hence the gas-liquid surface is not constrained, but free.

There are three essential features needed to properly model free surfaces: (1) A scheme is needed to describe the shape and location of a surface, (2) An algorithm is required to evolve the shape and location with time, and (3) Free-surface boundary conditions must be applied at the surface. The free surface problem has been formulated by using Lagrangian and Eulerian representation of continuum motion. In Lagrangian algorithms the nodes move with continuum, in Eulerian algorithms the nodes stay in place while the continuum moves through the stationary mesh or through Eulerian coordinate system. Non-Lagrangian algorithms deal with convection (advection) effect. The Lagrangian Grid Methods follow the Lagrangian formulation. The principal limitation of Lagrangian methods is that they cannot track surfaces that break apart or intersect. Arbitrary-Lagrangian-Eulerian (ALE) method exploit the merits of both Lagrangian and Eulerian formulation. Where as, Surface Height Method, Marker-and-Cell (MAC) Method, Surface Marker Method, Volume-of-Fluid (VOF) Method are purely based on Eulerian formulations. In Lagrangian or ALE-approaches, the free-surface always falls on the boundary of the computational domain. Hence, such methods do not pose any additional difficulty in applying complex boundary conditions. However these methods suffer the deficiency of requiring frequent remeshing. The choice of Lagrangian/ALE-method as opposed to VOF-variants, is based mainly on the type of problem and degree of precision to which the resulting free-surface is to be determined

(Sujatha et al., 2006). VOF technique tracks the fraction of each phase in every computational cell to extract the interface shape. The most successful of the various free surface methods is the VOF technique because of its simplicity and robustness.

Manipulating gas and liquid flows within networks of microchannels is crucial in the design and fabrication of microfiuidic devices. As the surface area to volume ratio increases, fluid/surface interactions become more significant with smaller fiuidic channels (Madou, 2002). Research on patterned surfaces revealed interesting phenomena that can be exploited to control liquid motions in microfiuidic devices. Hydrophobic and hydrophilic regions inside microchannels can be patterned through surface modification. However, fabrication of such patterned surfaces with selective surface characteristics is highly challenging task (Deval et al., 2004).

There have been a few studies reported for flow in patterned microchannels. Zhao et al. (2001) used surface directed liquid flow to create pressure sensitive switches inside channel networks. Self assembled monolayer chemistry is used in combination with multi-stream laminar flow and photolithography to pattern surface inside the microchannel networks. Kim et al. (2002) carried out experimental and numerical investigation for microchannel transient filling process with surface tension. A linear relationship between the dimensionless pressure and capillary number is observed. Their experimental observations indicate that flow blockage in the narrowest width channel is enabled by the surface tension and not by viscous effect.

Yang et al. (2004) discuss the method to characterize the surface energy inside a microchannel by monitoring the marching velocity of capillary meniscus. They formulated one-dimensional mathematical model and performed experimental validation of liquid filling in a capillary. Parylene and silicon nitride microchannels, which are fabricated using surface micromachining technology, are used for experimentation. The study indicates the influence of surface tension driven flow for fluid delivery in microfluidic systems.

Salamon et al. (2005) used finite element based numerical method to study a three-dimensional flow of Newtonian fluid in a 80 μm high microchannel with superhydrophobic lower and upper walls. They have shown a 40% flow enhancement over the smooth non-patterned surface and a apparent slip length of 5.4 μm. Byun et al. (2005) performed numerical visualization to investigate the effect of surface wettability in microchannel on the flow characteristics. The importance of hydrophobic and hydrophilic characteristics on a surface for the handling and control of liquid in the micro-systems are emphasised. The study shows the occurrence of flow instability in the flow path when the meniscus crosses hydrophilic/hydrophobic interface. Dalton et al. (2006) discuss issues in implementing superhydrophobic surfaces by nanostructured posts in a microchannel. The understanding and elimination of contact line movement effects on drag reduction is illustrated. Yang and Przekwas (1998) developed the computational methodology to model surface tension effects of multi fluid flow in ACE+MEMS CAD software. They present systematic validations against analytical solution for typical flows in MEMS devices. The unsteady motion of the free surface governed by the Hamilton-Jacobi evolution equation is solved on Eulerian grid using the Volume of Fluid (VOF) technique. Hirt and Nichols (1981) describe the concept of VOF method for treating complicated free boundary configurations. For simulation related to free surface flows, the water/air interface is characterized by surface tension and sharp changes in viscosity and density (Kothe et al., 1996). Among several general multiphase

models currently in use, the VOF model is the only multiphase model that enables identification of the interface clearly (Yian & Lawal, 2006).

Huang et al. (2006) have studied theoretically and numerically the capillary filling flows inside patterned surface microchannels. Two different patterned microchannel configurations - inner walls patterned with unequal contact angles; each inner wall divided into two equal segments having different contact angles have been considered for carrying out two-dimensional and three-dimensional simulations. Equivalent contact angle model based on surface energy method has been proposed for estimating capillary flows inside the patterned surface microchannels and they validated the model with traditional capillary rise theories.

A new method has been developed to modify the hydrophobic and hydrophilic nature of silicon surfaces by the use of 5-(4-Hydroxyphenyl)-10, 15, 20-tetra (p-tolyl) porphyrin self assembled monolayer (SAM) (Nayak et al., 2007; Mitra & Saha, 2008). The bare SiO_2 substrate exhibited a contact angle of 33 ±2° showing hydrophilic nature of the surface. In the case of Hydroxy-phenyl porphyrin SAM, the contact angle is found to increase up to 75 ± 3°, indicating a hydrophobic nature of the surface due to the formation of SAM on the SiO_2 surface.

Saha and Mitra (2007, 2008) presented numerical study on the surface dominated flow behavior in a channel with unsymmetrical distribution of surface characteristics with respect to channel axis. A three-dimensional (3D) numerical simulation of flow in patterned microchannels with alternate hydrophilic and hydrophobic surfaces at the bottom wall is considered. Hydrophilic surface induces the acute static contact angle while hydrophobic surface results in the obtuse static contact angle. Passive capillary driven flow phenomena in the microchannel is considered in their study. Capillary driven flows are purely governed by the forces associated with surface tension (Probstein, 1994) and offer positive flow enhancement effect.

3.1 Governing Equations

VOF Model

The simulations of the capillary flows in the patterned-surface microchannels are performed using a VOF method. In this method, a volume fraction transport equation is employed in addition to the continuity and momentum equations. Two phases (gas-liquid) are treated as a homogeneous gas-liquid mixture. The flow is considered to be laminar, non-gravity, incompressible, Newtonian and isothermal with velocity field V and governed by the Navier-Stokes and continuity equations, as provided here:

$$\nabla . V = 0 \tag{7}$$

$$\frac{\partial \rho V}{\partial t} + \nabla .(\rho VV) = -\nabla P + \nabla .(\mu(\nabla V + \nabla^T V)) + F_s \tag{8}$$

where V is the velocity of the mixture, P the pressure, t the time, F_s the volumetric force at the interface resulting from surface tension, and ρ, μ are the density and viscosity, respectively. In this equation the accumulation and convective momentum terms in every control volume (cell) balance the pressure force, shear force, and additional surface tension force F_s. Surface tension arises as a result of attractive forces between molecules in a fluid and it is represented as force acting only at the surface, which is required to maintain equilibrium in such instances.

The numerical simulation of free surface flows composed of two immiscible fluids involves two coupled tasks namely resolving the flow field and updating the position of the interface. This involves the application of SIMPLE algorithm (Patankar, 1980) and extending it to include the VOF methodology (Hirt & Nichols, 1981; Kothe et al., 1996). VOF method allows for the simulation of a mixture of two incompressible and immiscible fluids including surface tension effects. The VOF model includes the effects of surface tension along the interface between each pair of phases. The model can be augmented by the additional specification of the contact angles between the phases and the walls. The fluids under consideration are DI water as liquid and air as gas. The tracking of the interfaces between the phases is accomplished by the solution of a continuity equation for the volume fraction of any of the phases. The fields for all variables and properties are shared by the phases and represent volume-averaged values, as long as the volume fraction of each of the phases is known at each location. Thus the variables and properties in any given cell either represent one or a mixture of the phases, depending upon the volume fraction values. The distribution of the liquid phase is described by using a single scalar field variable, *F*, which defines the fraction of the liquid volume. Here, $F = 1$ represents liquid, $F = 0$ represents gas and $0 < F < 1$ represents the liquid/gas interface. The volume fraction distribution can be determined by solving the passive transport equation, given as:

$$\frac{\partial F}{\partial t} + V.\nabla F = 0 \tag{9}$$

where,

$$F = \frac{\text{cell volume occupied by liquid}}{\text{total volume of the control cell}} \tag{10}$$

The mixture's physical properties are derived from that of the two phases through the volume fraction function. In particular, the average value of any volume-specific quantity, ρ in a computational cell can be computed from the value of *F* in accordance with:

$$\rho = F\rho_2 + (1-F)\rho_1 \tag{11}$$

where the subscripts 1 and 2 represent the gas phase and the liquid phase, respectively. For an intensive quantity, μ, the effect of density can be included as given below:

$$\mu = (F\rho_2\mu_2 + (1-F)\rho_1\mu_1)/(\rho_1+\rho_2)/2 \tag{12}$$

The surface tension model follows the continuum surface force (CSF) model proposed by Brackbill et al. (1992). The surface tension is specified as a source term F_s in Eq. 8 according to the CSF model:

$$F_s = \frac{\rho\sigma\kappa\nabla F}{(\rho_1+\rho_2)/2} \tag{13}$$

The surface tension is taken to be constant along the surface and only the forces normal to the interface are considered. According to the CSF model, the surface curvature κ is computed from local gradients in the surface normal to the interface, which is given as:

$$\kappa = \frac{1}{|n|}\left(\left(\frac{n}{|n|}\cdot\nabla\right)|n| - \nabla\cdot n\right) \tag{14}$$

where $n = \nabla.F$ is the normal vector. Wall adhesion is included in the model through the contact angle:

$$\hat{n} = \hat{n}_w \cos\theta + \hat{t}_w \sin\theta \tag{15}$$

where n is the unit vector normal to the surface, $\hat{n} = \frac{n}{|n|}$, $\hat{n}_w$ and $\hat{t}_w$ represents the unit vector normal and tangent to the wall, respectively. The interface needs to be constructed based on the computed value of the volume fraction with the application of interpolation schemes for the identification of the interface. An upwind scheme with the piecewise linear interface construction (PLIC) method, is adopted for surface reconstruction (Kothe et al., 1996). In the PLIC scheme, the liquid-gas interface is assumed to be linear and can take any orientation within the cell. The reconstructed interface is represented by line segments in a two-dimensional flow and by an arbitrary polygonal face for three-dimensional flows. The reconstruction is required at every time step to include the necessary back-coupling of surface forces to the momentum equations as well as flux calculations. Equations (7) – (15) are solved iteratively to obtain the liquid volume fraction and the velocity field solution under appropriate initial and boundary conditions.

For the channel height of 100 μm selected in this study, the Bond number (Bo), $\rho g H^2/\sigma$, and Capillary number (Ca), $\mu U/\sigma$, are much less than unity. Hence, the effects of gravity and dynamic contact-angle are not taken into account in the present study.

The solution of the passive transport equation in conjunction with the standard conservation equations in CFD-ACE+ requires three related actions: (1) Compute mixture properties, (2) Reconstruct the fluid-fluid interface in each cell, and (3) Determine the contribution of the secondary fluid flux to the equations for conservation of mass, momentum, energy and volume fraction. The classification of the VOF method as a volume-tracking method follows directly from the use of the single scalar variable F to describe the liquid distribution and to solve for the liquid volume evolution. One consequence of the purely-volumetric representation of the phase distributions is that there is no unique definition of the interface between the two phases. As such, if the location of the interface is required for any modeling, computational, or visualization purpose, then it must be dynamically reconstructed from the F distribution. In CFD-ACE+, surface reconstruction is a prerequisite for determining the flux of fluid two from one cell to the next and for determining surface curvatures when the surface tension model is activated. In the PLIC scheme (Fig. 6), the liquid-gas interface is assumed to be planar and allowed to take any orientation within the cell, and will therefore generally have the shape of an arbitrary polygonal face. The facet in a cell is fully defined by specifying: (i) the spatial orientation of the infinite plane that contains the facet; and, (ii) the location of a point within the cell through which the infinite plane passes. The orientation is specified by specifying the outward-pointing unit normal of the infinite plane, and the sense of the normal is here arbitrarily chosen so that it points out of the liquid phase and into the gas phase. The unit normal of the plane is determined by assuming that it is parallel to the gradient vector of F. The gradient of F is determined from the local distribution of F in a set of cells which includes the target cell and all its immediate

neighbors. The location of the anchor point is determined by finding the infinite cutting plane perpendicular to the unit normal of the infinite plane that truncates the correct liquid volume from the cell, in that it satisfies the condition:

$$V_{cut} = F.V_c \tag{16}$$

where V_{cut} is the volume of the cell truncated by the cutting plane, V_c is the volume of the whole cell, and F is as defined above. In the PLIC scheme, each cell has a unique surface normal that can be used to compute the surface curvature from cell to cell. This calculates and adds surface tension forces for the free surfaces.

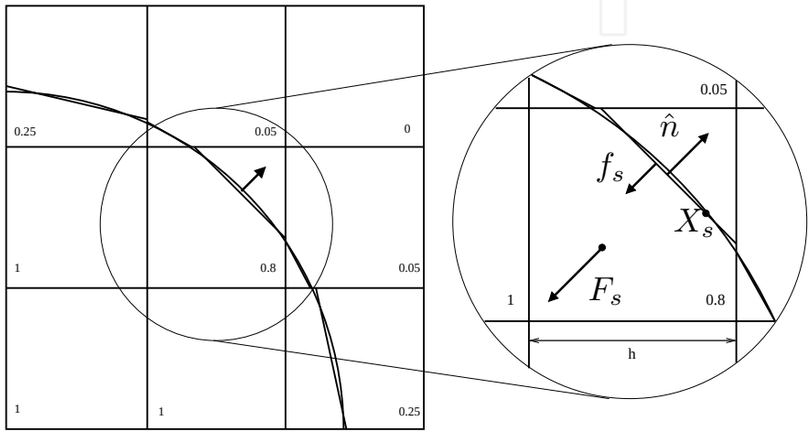

Figure 6. PLIC reconstruction scheme

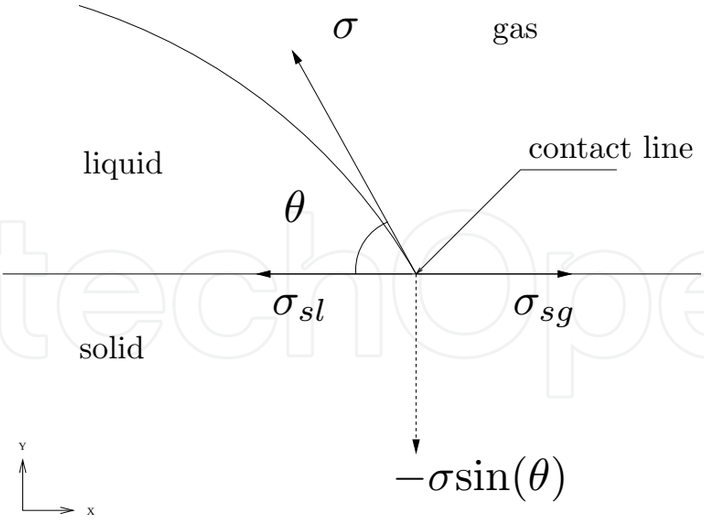

Figure 7. Contact angle

Lucas-Washburn Model

Analytical solution for the propagation of a liquid in a channel is derived in the following sections. The analytical solution is based on the Navier-Stokes equation for incompressible, quasi-steady, laminar, Newtonian 2D horizontal flow,

$$-\frac{\partial P}{\partial x} = -\mu \frac{\partial^2 u}{\partial y^2} \tag{17}$$

where P is the pressure in the fluid at x, μ , is the viscosity of the fluid, u is the velocity of the fluid. For a fully developed capillary driven flow, the analysis on the balance of viscous force, surface tension force, and gravitational force yields the classical Lucas-Washburn equation on the penetration length, L, evolution with time, t (Washburn, 1921).

For static wetting of a liquid between two surfaces, the minimization of surface area of a liquid may result in a curved interface. The general Young's-Laplace equation describes the relation for the pressure difference across the interface as (Fig. 7):

$$\Delta P = \sigma \left(\frac{1}{\mathrm{R}_1} + \frac{1}{\mathrm{R}_2} \right) \tag{18}$$

where ΔP is the pressure difference, σ is the liquid surface tension, and R_1 and R_2 are the radius of curvature of the interface in directions perpendicular and parallel to the liquid stream. For a two-dimensional channel $R_2 = \infty$.

Therefore,

$$\Delta P = \sigma \frac{1}{\mathrm{R}} \tag{19}$$

From Fig. 8,

$$R = \frac{h}{2\cos\theta} \tag{20}$$

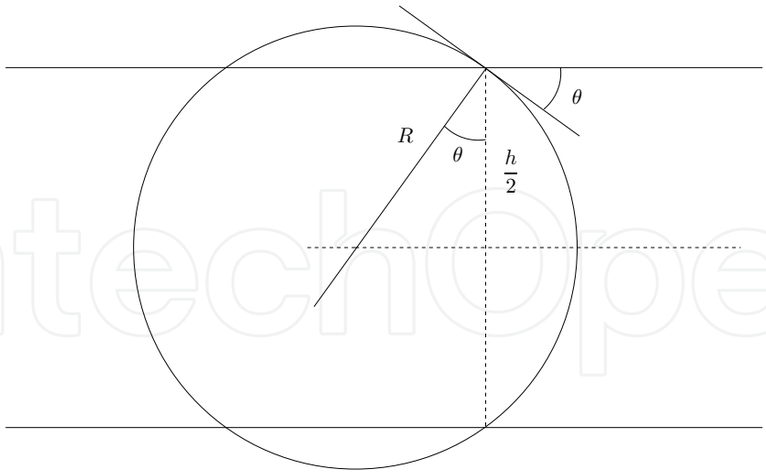

Figure 8. Meniscus in channel

For steady 2D Poiseuille flow,

$$u_{avg} = \frac{1}{12\mu} \frac{\Delta P}{L} h^2 \tag{21}$$

Also,

$$u_{avg} = \frac{dL}{dt} \tag{22}$$

Thus,

$$L = \left(\frac{ht\sigma\cos\theta}{3\mu} \right)^{\frac{1}{2}} \tag{23}$$

It shows that the flow time is inversely proportional to the surface tension, separation distance, and the cosine of the wetting angle, and directly proportional to the viscosity and the square of the flow distance.

Reduced Order Model

Consider a microchannel, height of which is h, initially is filled with liquid (density ρ, dynamic viscous coefficient μ) length of L_0. The contact property between the liquid and channel wall is defined by surface tension coefficient σ and contact angle θ. An overhead pressure is ΔP. For a passive capillary filling process, ΔP=0. The surface tension force and the pressure overhead drive the liquid free surface in the microchannel.

At time t, the liquid length is denoted L, and average velocity is denoted u. The velocity profile is assumed two-dimensional Poiseuille. The momentum of the liquid column may be written as ρ hLu. The momentum conversation may be expressed as momentum change is balanced by the sum of the surface tension force, pressure overhead and wall viscous force.

$$\frac{d}{dt}(\rho hLu) = 2\sigma\cos\theta + \Delta Ph - \frac{12\mu L}{h}u \tag{24}$$

The term denoting the momentum change is often omitted, with quasi-steady state assumption (Zeng, 2007). Considering in microfluidics that (1) the Reynolds number is always very small; and (2) the surface tension force is always dominant; this quasi-steady state assumption is valid except for the initial starting stage that is highly transient. In the reduced order model a transient solution is derived accounting for all terms in the equation above. Noting u = dL/dt, the equation above can be re-written as

$$\frac{d^2}{dt^2}L^2 + B\frac{d}{dt}L^2 = A \tag{25}$$

where,

$$A = \frac{4\sigma\cos\theta + 2\Delta Ph}{\rho h}, B = \frac{12\mu}{\rho h^2} \tag{26}$$

Considering initially the liquid holds column length of L_0 and with zero velocity, the transient solution of the capillary filling problem is given below:

$$L = \left(\frac{A}{B^2}exp(-Bt) + \frac{At}{B} + (L_0^2 - \frac{A}{B^2}) \right)^{\frac{1}{2}} \tag{27}$$

$$u = \frac{A(1-exp(-Bt))}{2BL} \tag{28}$$

where t is the time of the filling process, L is the position of free surface front, u is the average filling speed.

3.2 Numerical Simulation

Physical Problem

In Fig. 9 geometry of the microchannel model is shown. The channel considered here is a three-dimensional straight channel. The cross sectional area of the channel is 100 μm x 100 μm. The model consists of a single straight segment of 1000 μm in length. Alternate patterns of hydrophilic and hydrophobic surface arrangement is shown on the bottom wall of the channel geometry, to account for the surface tension effect on the flow.

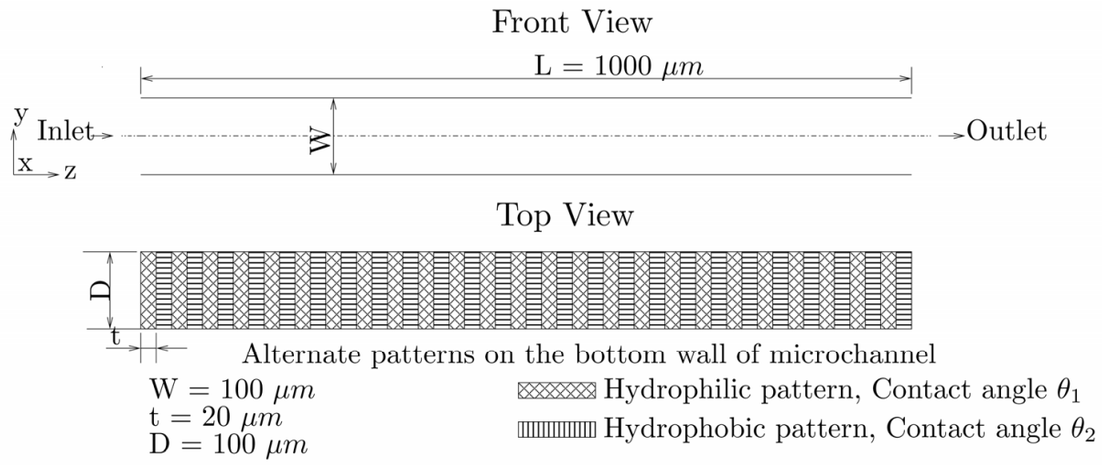

Figure 9. Geometry of microchannel

Initial and Boundary Conditions

Initially, at time t = 0, the liquid meniscus position in the channel is set as 1 μm. No slip boundary condition is imposed on all the walls and the boundary conditions for the surface affinity is described by the contact angle. The contact angle θ_1 = 30°, θ_2 = 120° is specified on the bottom walls of the channel as shown in Fig. 9. A contact angle of 0° is specified on all the other walls as it is considered to be fully wet. Passive capillary filling process is considered by specifying a constant pressure (atmospheric) at channel inlet and outlet. A liquid volume fraction (LiqVOF) value of unity and zero is specified at channel inlet and outlet for all the cases.

Numerical Technique

The channel geometry is created and meshed using CFD-GEOM modeler (ESI CFD Inc., 2007). Structured grid is used for simulations. Structured grid having having 100000 (20x20x250) cells is used for the three-dimensional simulations. CFD software CFD-ACE+ based on finite volume method is used for the time dependent simulations. Flow and free surface (VOF) modules of CFD-ACE+ are used for analysis. Second-order PLIC surface reconstruction method with surface tension effect is specified for VOF with explicit time integration scheme. Explicit option is selected as it exhibits greater stability and better

convergence, but slightly lower accuracy as compared to the implicit scheme. However, for an accurate resolution of the interface and prediction of the interface shape and its location, this is the preferred option. Euler (1st order) scheme is applied for time accuracy. A target Courant-Friedrich's-Lewy (CFL = $|v|\ \delta t/h$) number of 0.1 is applied for numerical stability of the simulation. This would allow the interface to cross 10 % of the width of a grid cell during each time step in a VOF computation. Upwind scheme is used for spatial differencing. Semi-implicit method for pressure-linked equations consistent (SIMPLEC) algorithm is adopted for pressure-velocity coupling and pressure correction. The conjugate gradient squared plus preconditioning (CGS+Pre) solver (ESI CFD Inc., 2007) for velocity while algebraic multigrid (AMG) solver is used for pressure correction. Initial time step of 1.0E-07 s is selected and the VOF module is allowed to automatically adjust the time step size based on the CFL number and interface velocity. An automatic time step option automatically ensures stability in the CFD-ACE+ solver. Each case is given 100 iterations per time step with a convergence criteria of 0.0001 to control the iterative solution process. The solver quits the iterative procedure when the maximum relative difference between the computed values of variables in two successive iterations is smaller than the specified convergence criteria. The physical properties used for simulations are provided in Table 2.

Physical property	Water	Air
Density *(kg/m³}*	1000	1.1614
Viscosity (*Pa.s*)	1.0 x 10^{-3}	1.846 x10^{-5}
Surface Tension *(N/m)*	75 x 10^{-3}	-

Table 2. Properties used in simulation

Results and Discussion

The snapshot image of the meniscus front is shown in Figs. 10. It shows clearly the meniscus profile obtained on all the walls due to the surface tension effect. It is also observed that the meniscus is symmetric about the y-z coordinate plane and unsymmetrical about x-z coordinate plane passing through the channel axis.

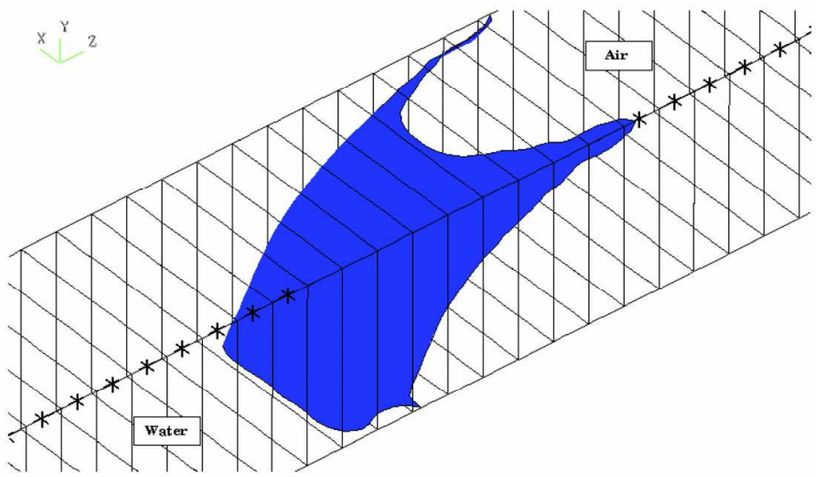

Figure 10. The three-dimensional snapshot image of meniscus front (θ_1 = 30°, θ_2 = 120°)

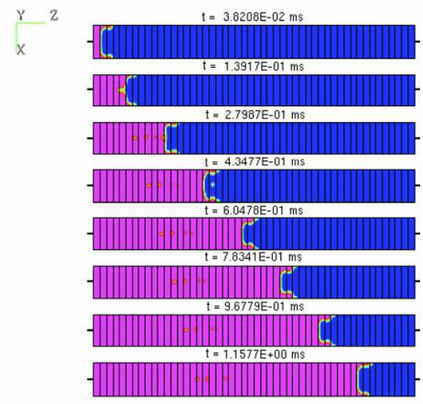

(a) Bottom View

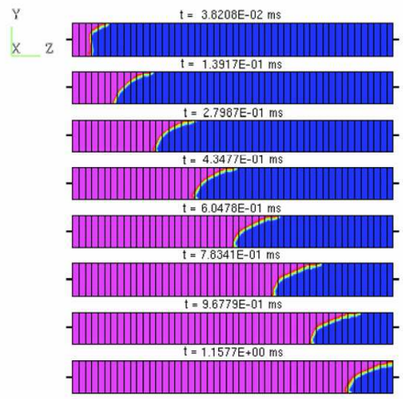

(b) Front View

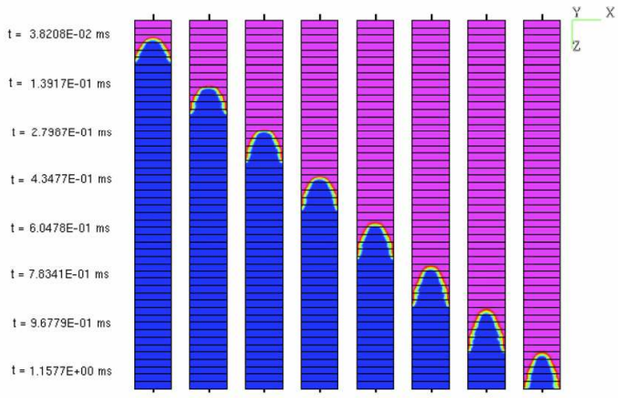

(c) Top View

Figure 11. The snapshot image of the time evolution of meniscus front (θ_1 = 30°, θ_2 = 120°)

The snapshot image of the time evolution of meniscus front on all the walls in the microchannel is shown in Fig. 11. The pink background indicates the liquid volume fraction (LiqVOF=l) as the fluid advances in the microchannel while blue background indicates air (LiqVOF=0). As the meniscus is symmetric about the y-z coordinate plane passing through the channel axis, the front view of the meniscus is only shown in the figure. It is observed that due to the alternate θ_1 = 30°, θ_2 = 120° contact angle specified on the bottom wall the meniscus shape is not symmetric about the x-z coordinate plane passing through the channel axis. The unsymmetrical distribution of surface characteristics with respect to channel axis results in the stretching of the meniscus. This is due to pronounced retarding flow effect on the bottom wall and stretching of the meniscus on the top wall. As the fluid at the bottom wall traverses alternately from hydrophilic region to hydrophobic region, the curvature of the meniscus changes very sharply and large velocity gradients are observed at the wall. This gives rise to high flow instability in the microchannel. It is therefore possible to manipulate fluid flow by controlling, the size of the patterned surface (Saha & Mitra, 2008). Such phenomena will find applications for performing biological reactions in microfluidic devices using the capillary flow. All biological reactions need sufficient incubation time to complete the reaction. It is believed that sufficient incubation time necessary for reaction to proceed will be inherently available in the patterned microchannel.

The biological fluid will come in contact with surface, which will alternately assist and retard its flow. The region where the flow is retarded can be used for the reaction zone.

Grid Dependency and Validation

Validation of the numerical results with analytical solution has been carried out for non-patterned two-dimensional microchannel 100 μm height and 2000 μm length with contact angle θ = 0° for DI water and ethanol. The time evolution of meniscus displacement is considered as the parameter for validating the numerical results. Figure 12 shows the comparison of meniscus displacement obtained numerically with the analytical solution based on a reduced-order model (Zeng, 2007) for DI water and ethanol. Good agreement between numerical and analytical results is observed for DI water and the results deviate by about 5% for ethanol. It is to be noted that, in general, the meniscus displacement in a capillary follows the Lucas-Washburn equation which predicts that the distance travelled by the meniscus to be proportional to $\sqrt{t}$. The Lucas-Washburn equation is an asymptotic model for large times and is derived based on the balance of capillary and friction forces when the influence of other forces during the initial transients become insignificant (Stange et al., 2003). This quasi-steady state assumption is valid except for the initial starting stage which is highly transient. The validation studies reported in literature (Yang et al., 2004; Yang & Przekwas, 1998; Huang et al., 2006) are observed for very large time scale (t ~ sec). However, the time scale considered for the present study are in the range of milli seconds (t ~ ms). Therefore, the plots in Fig. 12 do not necessarily obey the Lucas-Washburn equation, but a reduced-order model (Zeng, 2007) which accounts for the inertia is found to be a better choice for the representation of the meniscus displacement under the given conditions. Hence, deviation between the predicted numerical results and the Lucas-Washburn model can be justified and it is also observed that the inertia effects are more prominent for DI water than compared to ethanol.

When performing the VOF free surface simulations, the generation and the choice of grid are generally of great importance. It takes an enormous amount of time to perform any VOF simulation and the simulation time increases with the grid refinement. The simulation time for 10 x 200 grid is typically around 45 minutes on a 2.4 GHz AMD 64 Opteron processor running Linux with an access to 4 GB RAM. It is to be noted that with the increase in the grid resolution in every direction by a factor of 2, the calculation time in a two-dimensional grid increases by a factor of 8. Also, the time step under such condition needs to be decreased by a factor of 2 in order to fulfill the CFL stability criteria.

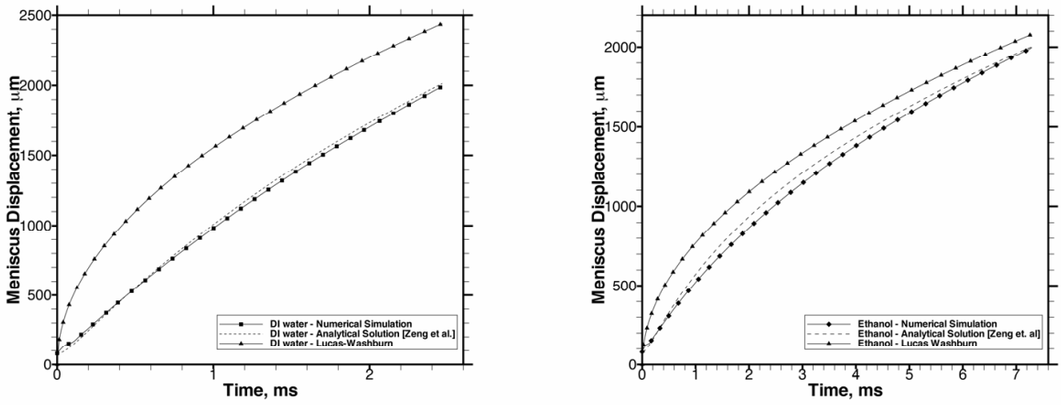

(a) DI water (b) Ethanol

Figure 12. Validation of numerical model with analytical solution (Zeng, 2007)

Figure 13 shows the comparison of coarse and fine grid CFD-ACE+ results for three-dimensional microchannel. It is observed that by increasing the grid resolution, a sharp interface profile of the meniscus is obtained, where as this also has a corresponding influence in under predicting the meniscus displacement. As the VOF method is based on geometric back projection (ESI CFD Inc., 2007) to calculate fluxes, so the solution depends on the grid size. This is contrary to what one would expect, the accuracy obtained from the present VOF code deteriorates with the increase in the grid resolution (Raessi et al., 2007). With the inclusion of surface tension in the VOF model, a balance has to be made between the fine grid and the local accuracy, as finer grid size results in higher spurious velocities. However, it may be noted that, grid refinement affects the dynamics of capillary flows only slightly, allowing coarse grids to be a good basis for qualitative and quick simulations (Trutschel & Schellenberger, 1998).

To compare result of the present VOF algorithm with other available commercial codes, we have run similar test cases with Fluent 6.3.21 which also has a VOF module. However, limited comparison of various VOF codes are available in open literature, which is mainly due to simulation dependence on quality of code and undocumented features of algorithms (Bourago, 2002). Figure 14 shows the comparison of CFD-ACE+ and Fluent results for different grid sizes for two-dimensional microchannel. It is again observed that, both the codes under predict the meniscus displacement with decrease in mesh size.

Figure 15 shows the comparison of CFD-ACE+ and Fluent results with analytical solution for a two-dimensional microchannel (40 μm x 7000 μm) with black ink as working fluid with contact angle θ = 36°. The results obtained with both CFD-ACE+ and Fluent show excellent agreement and provide confidence on the current model formulation. It is observed that CFD-ACE+ predicts higher meniscus displacement than compared to Fluent with increasing time. The minor differences observed in the results are primarily due to different solver settings used during the simulation. The cpu time for coarser grids in CFD-ACE+ is lower compared to Fluent, whereas when the grid size is refined, the CFD-ACE+ simulations get extremely slower compared with Fluent simulations. To reduce the cpu time, both the commercial codes offer alternative time step selection, viz., automatic time step (CFD-ACE+) and non-iterative time advancement (Fluent). Considerable amount of time saving is obtained when such features are employed in simulation.

It is also observed that when large number of grid cells are used near the wall, in particular the small ones, compared to the rest of the domain, it results in an unstable solution. This is due to the fact that, grids with high aspect ratios affect the accuracy of the surface-reconstruction algorithm. Moreover, it should be noted that, it is difficult to accurately approximate the long time evolution of moving interfaces with VOF algorithm (Li et al., 2007; Erickson, 2005). This tends to limit the ability of these methods to track capillary driven flows over long distances. To ascertain the accuracy of the method, VOF simulations for a microchannel with very high length to width ratio is also conducted. Figure 16 shows the comparison of meniscus displacement predicted by VOF method for a microchannel 100 μm x 10000 μm with DI water as working fluid (contact angle θ = 0°) with analytical solution. The meniscus displacement results indicate a 10 % deviation with analytical solution when time is increased asymptotically by both CFD-ACE+ and Fluent. However, as the solution domain considered in the present study are for short time scales, the predicted results are fairly accurate and acceptable.

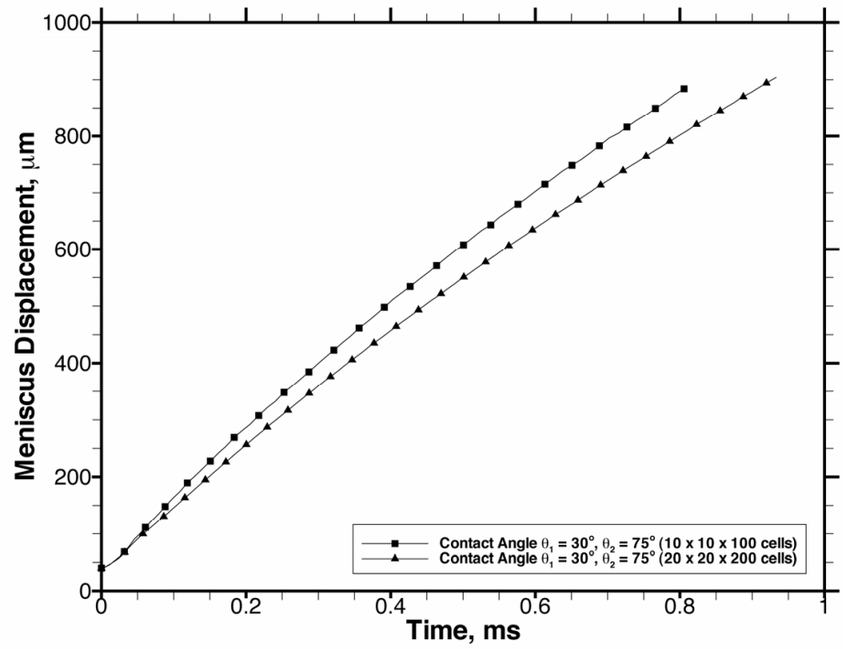

Figure 13. Comparison of coarse and fine grid CFD-ACE+ results (3D)

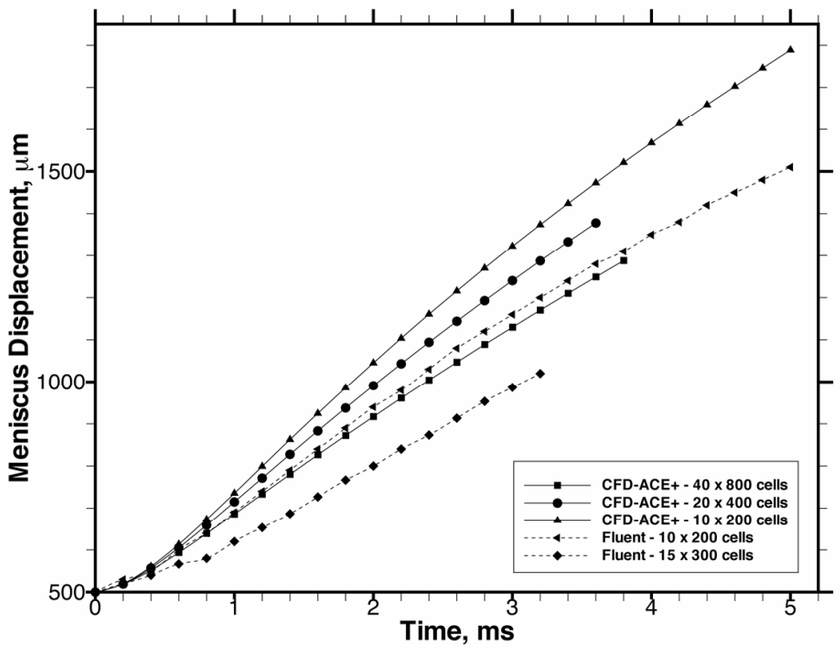

Figure 14. Comparison of coarse and fine grid CFD-ACE+ and Fluent results (2D)

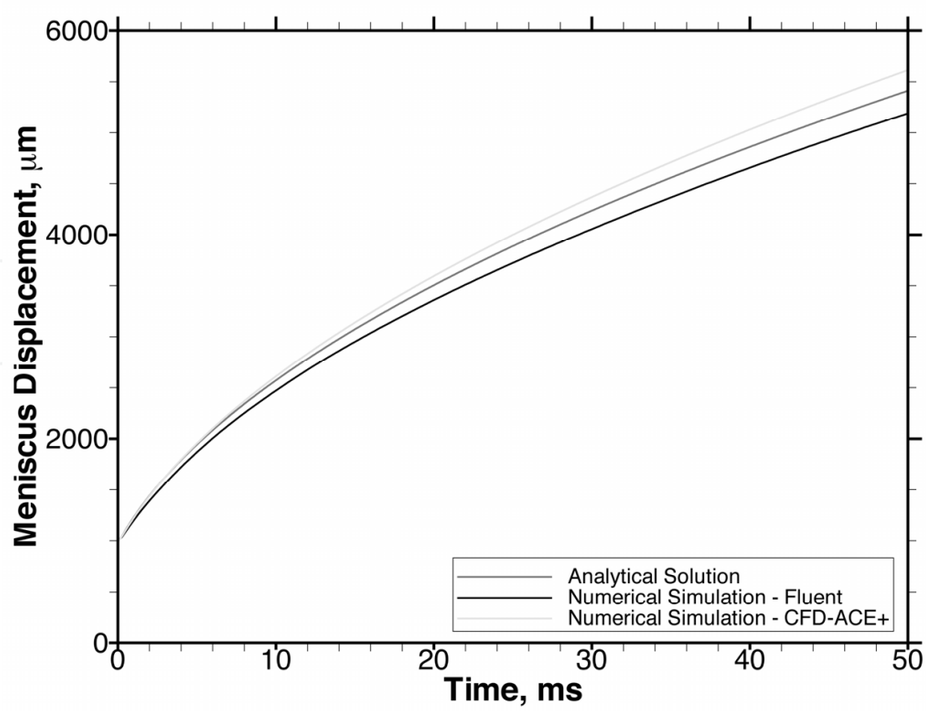

Figure 15. Comparison of CFD-ACE+ and Fluent results with analytical solution (2D)

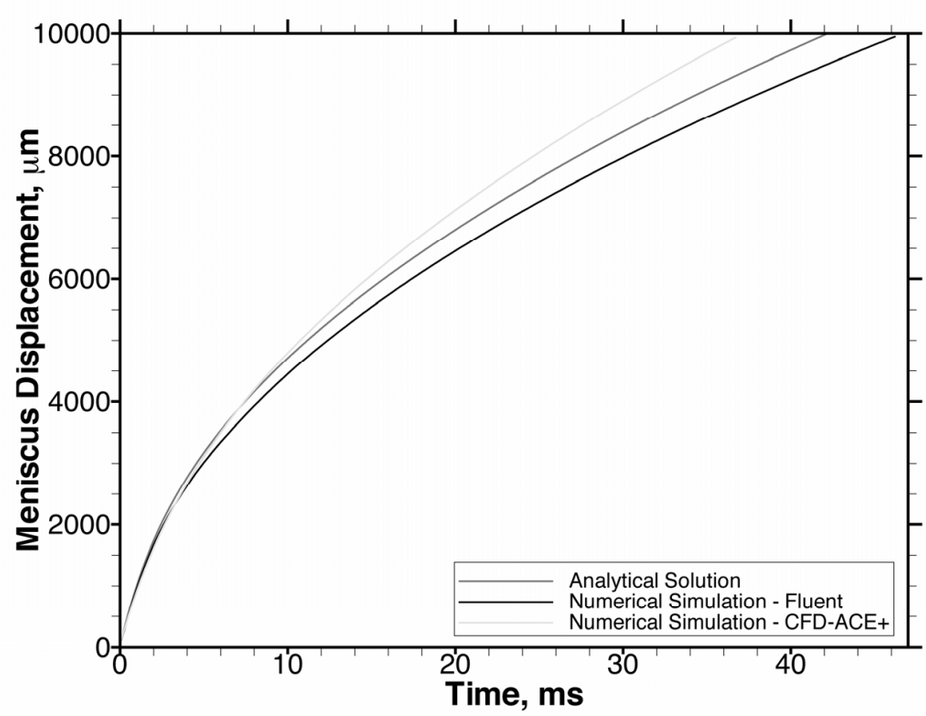

Figure 16. Comparison of CFD-ACE+ and Fluent results with analytical solution for very long microchannel (2D)

4. Fluid Structure Interaction

The dynamic interaction between an elastic structure and a fluid has been the subject of intensive investigations in recent years (Dargush & Banerjee, 1990; Fan & Tijsseling, 1992; Fujita, 1990; Lui & Lou, 1990). Since analytical solutions are available only for very simple problems, numerical approaches, which can be formulated in time or frequency domain, have to be employed. Vonestorff and Antes (1991) investigated the coupled fluid-structure systems subjected to dynamic loads using the finite element and boundary element methods. Similar method is used by Olson and Bathe (1985) to analyze fluid-structure interaction. Many researchers have attempted to derive variational principles for different classes of the fluid-structure interaction problems. Pinsky and Abboud (1989) proposed two mixed variational principles for transient and harmonic analyses of non-conservative coupled exterior fluid-structure interaction systems. Kock and Olson (1991) presented a finite element formulation directly derived from a variational indicator based on Hamiltons principle. Zeng and MacCamy (1992) developed an energy-based symmetric coupled finite element and boundary integral method which is valid for all frequencies. Seybert et al. (1993) employed Ritz vectors and eigenvectors along with a combination of finite element and boundary element methods to reduce the problem size. Several finite element studies have considered the gravity and free surface effects along with the fluid structure interaction. Wilson and Khalvati (1983) incorporated the gravity and the free surface effects in a displacement-based method with rotational constraints. They demonstrated results for both static and dynamic floating body problem. Their method necessitates the use of a reduced integration scheme to prevent element locking.

Moondra et al. (2006) numerically studied the flow through a microchannel with an elastic membrane and discuss the effects of various parameters - such as elasticity of the membrane, viscosity of the liquid, and the geometry of the elastic membrane on the displacement of the tip of the membrane and its maximum shear stress.

4.1 Governing Equations

Commercial software, COMSOL, is used to analyze the fluid-structure interaction as it provides a strong coupling between the dynamics of fluids and the dynamics of structures. At each computational step, the fluid flow field and the structure evolve as a coupled system. The interaction forces are immediately accounted for and their resultant motions enforced in each step.

Here, the flow field is solved in a continuously deforming geometry using the arbitrary Lagrangian-Eulerian (ALE) technique. The fluid flows in the channel from left to right. An obstacle, however, forces it into the narrower path in the upper portion of the channel, and a force resulting from the viscous drag and fluid pressure is imposed at the walls. Because the structure is made of deformable material, it bends under the applied load. Consequently, the fluid flow also follows a new path, and solving the flow in the original geometry can generate incorrect results. The ALE method handles the dynamics of the deforming geometry and the moving boundaries with a virtual moving grid. It computes new mesh coordinates on the channel area based on the movement of the boundaries of the structure. It reformulates the Navier-Stokes equations that solve the flow. The structural-mechanics portion of the model does not require the use of ALE, and it solves in a fixed coordinate system as usual. However, the strains computed are to be used for the computation of the deformed coordinates with ALE.

Following are the governing equations, which are solved using ALE technique:

$$\rho\frac{\partial V}{\partial t}-\nabla.((-p)I+\eta(\nabla V+(\nabla V)^{T}))+\rho((V-V_{m}).\nabla)V=F \tag{29}$$

$$\nabla.V=0 \tag{30}$$

where ρ is the fluid's density, V = (u, v) is the velocity field of the flow, V_m = (u_m, v_m) is the coordinate system velocity, p is the fluid pressure, I is the unit diagonal matrix, and F = (f_x, f_y) is the volume force affecting the fluid.

4.2 Numerical Simulation

Physical Problem

A two-dimensional microchannel is considered here with different geometries, as shown in Figs. 17 and 18. The width of the channel is 100 μm and length is 300 μm. A vertical structure is located 100 μm away from the channel inlet. The fluid in the channel has the property of water with a density of 1000 kg/m^3 and dynamic viscosity of 0.001 Pa.s (unless otherwise stated). The vertical structure is a flexible material with a density of 7850 kg/m^3 and Youngs modulus of 20 kPa (unless otherwise stated).

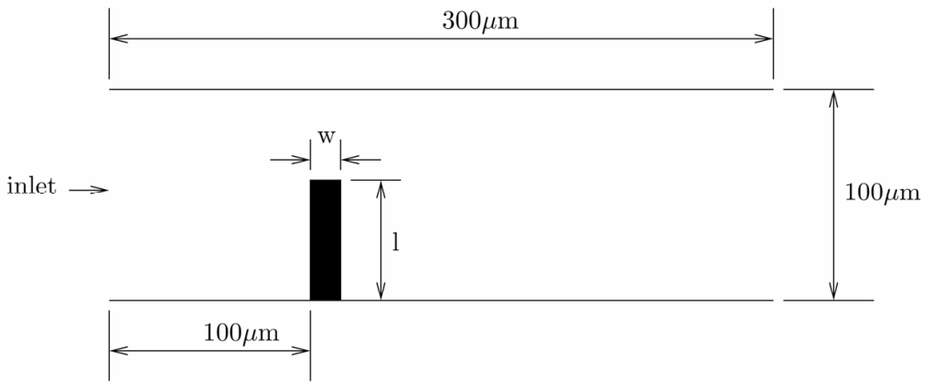

Figure 17. Schematic diagram of the microchannel with elastic structure of height 1 and width w (Case 1)

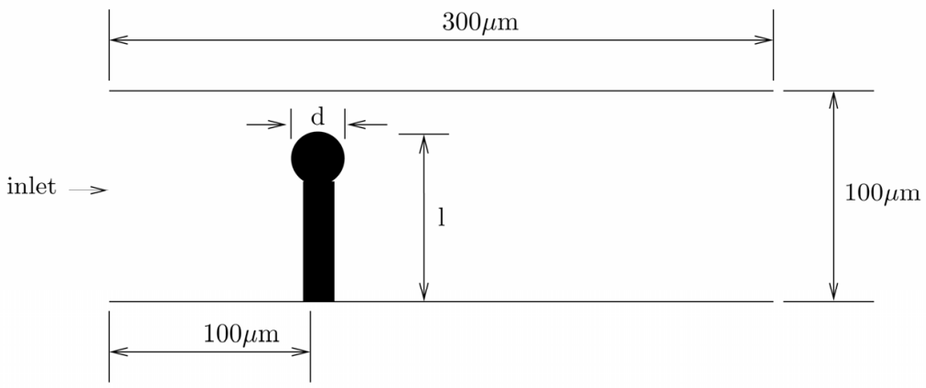

Figure 18. Schematic diagram of the microchannel with elastic structure of height 1 and a semicircular top of diameter d (Case 2)

Initial and Boundary Conditions

At the entrance the flow is fully developed with a parabolic velocity profile, but the flow amplitude changes with time. At first it increases rapidly, reaching its peak value at 0.215 s; thereafter the flow gradually decreases to its steady-state value of 5 cm/s. The centerline velocity u_{in} in the x-direction with the steady-state amplitude U is given as,

$$u_{in} = \frac{Ut^2}{\sqrt{(0.04 - t^2)^2 + (0.1t)^2}} \tag{31}$$

It is assumed, there is no effect of gravitation or other volume forces affecting the fluid, so F = 0. Pressure is specified at the channel outlet, the condition is p = 0. For all other boundaries, no-slip condition is imposed. However, on boundaries where the fluid forces the structure to deform, the no-slip condition means that the fluid moves with the velocity of the adjacent fluid-structure boundary.

Numerical Technique

The structural-mechanics part of the model is solved with reference to the fixed coordinates using a plane stress analysis. The deformation of the structure resulting from the fluid can be large. Therefore, to improve the accuracy of the computation of deformations, strain values are given by Green strains. The bottom of the structure is fixed with the channel and hence its movement is restricted in all directions. All other boundaries can move freely, and there is an applied load on these boundaries. The applied load consists of the viscous drag and the pressure of the surrounding fluid.

Results and Discussion

Figures 19 and 20 show the streamline plot for the two cases considered here. It is observed that the structure with a round tip is deformed further and it results in vortex formation at the tip.

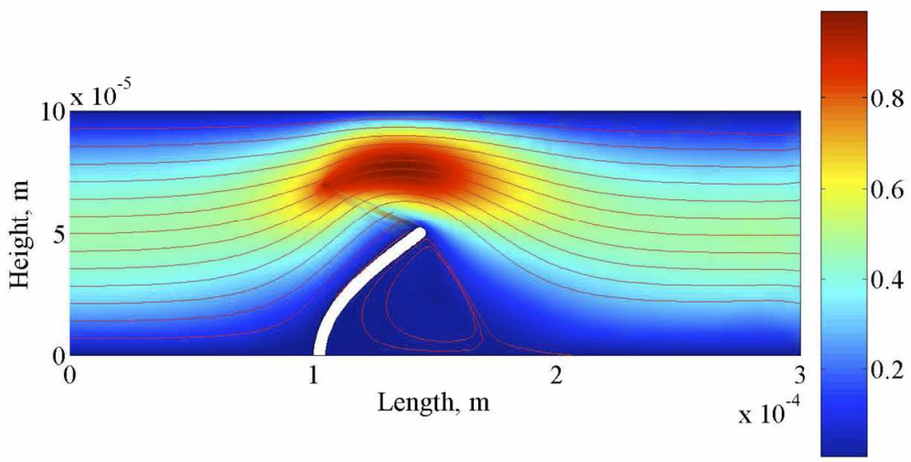

Figure 19. Streamlines for 1/w = 14. Color indicates velocity magnitude. (Case 1)

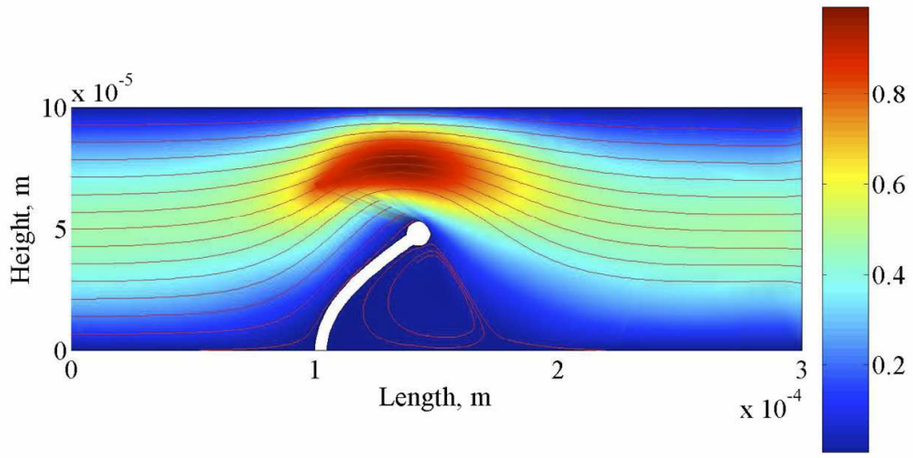

Figure 20. Streamlines for 1/d = 7. Color indicates velocity magnitude. (Case 2)

The variation in the tip deformation is shown in Fig. 21 for different 1/w ratios and in Fig. 22 for different 1/d ratios. It is observed that for all cases the tip deformation increases rapidly for a few initial seconds and then it becomes constant for all subsequent times. The displacement maxima is observed to be slightly higher for the round tip structure.

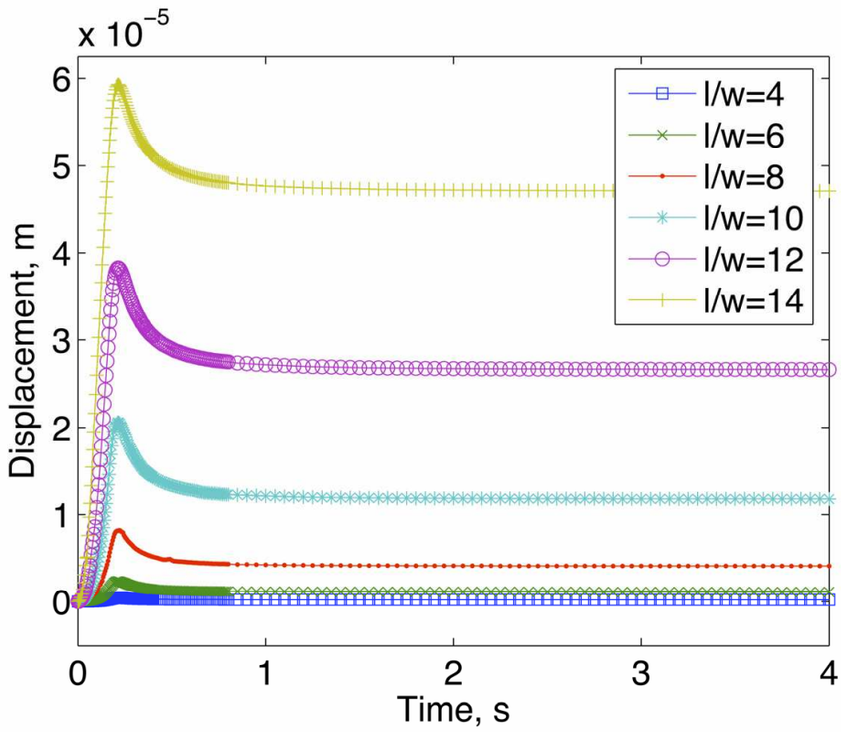

Figure 21. Transient response of tip displacement for various 1/w ratios (Case 1)

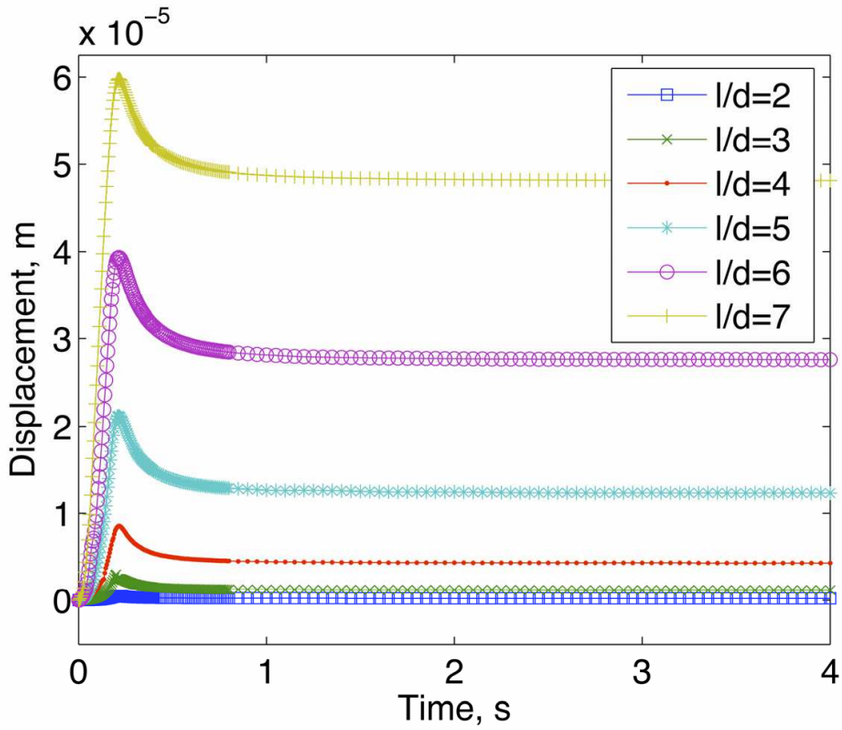

Figure 22. Transient response of tip displacement for various 1/d ratios (Case 2)

It is also observed that, the maximum shear stress increases non-linearly with 1/w and 1/d ratio for Cases 1 and 2. However, for the round tip structure the magnitude of maximum shear stress is higher than the flat tip. This has direct impact in the design of the structural membrane embedded in the microchannel.

5. Summary

Microfluidic simulation of flows in microchannels was presented in this chapter. Electroosmotic driven flows in three-dimensional serpentine microchannel was investigated with non-uniform zeta potential. Free surface flows in patterned microchannel having alternate hydrophilic/hydrophobic on the bottom wall was discussed for a three-dimensional microchannel. Flow through a two-dimensional microchannel with an embedded elastic structure was studied

- It is observed that vortices are developed at the straight portion of the microchannel due to electroosmosis for the channel side walls subjected to variable zeta potential. The core of the vortices shifts when variable zeta potentials are applied at both the side walls of the channel. Flow control in the serpentine microchannel by regulating the zeta potential at the bend has also been demonstrated. Formation of additional vortices at the top left and bottom right corners of the serpentine microchannel has been observed at the semi-circular bend for very low values of applied zeta potential.
- The unsymmetrical distribution of surface characteristics with respect to channel axis results in the stretching of the meniscus in patterned microchannel with alternate layers of hydrophilic and hydrophobic surfaces at the bottom wall. Non-symmetric meniscus

profiles are obtained by changing the contact angles of the hydrophilic and hydrophobic surfaces. Flow instability is found to be increased in the microchannel as the fluid at the bottom wall traversed alternately from hydrophilic region to hydrophobic region. The capillary flow phenomena in the microchannel indicate that flow control is possible by surface patterning the channel walls for applications in microfluidic devices.

- A parametric study for different geometries is conducted to study the effect of elasticity of the structure and viscosity of the fluid on the maximum shear stress developed in the structure and the maximum displacement of the tip of the structure. It is observed that stress is more for taller structures. The maximum shear stress in the structure are not affected to a large extent by the change in elasticity of the structure but increase with increasing viscosity of the medium.

6. Acknowledgment

The support of Suman Mashruwala Advanced MicroEngineering Laboratory, IIT Bombay is highly appreciated.

7. References

Bourago, N. G. (2002). A survey on Contact Algorithms. *Proceedings of Workshop Grid Generation: Theory and Applications,* Edited by S.A. Ivanenko & V.A. Garanzha, Computing Centre of RAS, Moscow, pp. 42-59. 18

Brackbill, J. U.; Kothe, D. B. & Zemach, C. (1992). A continuum method for modeling surface tension. *J. Comput. Phys.,* 100, pp. 335-354.

Brant, J. A.; Johnson, K. M. & Childress, A. E. (2005). Examining the electrochemical properties of a nanofiltration membrane with atomic force microscopy. *Journal of Membrane Science,* 2, pp. 286-294.

Buie, C. R.; Banin, Y.; Chuyang, T.; Santiago, J. G.; Prinz, F. B. & Pruitt, B. L. 2006. A microfabricated direct methanol fuel cell with integrated electroosmotic pump. *19th IEEE International Conference on Micro Electro Mechanical Systems,* Istanbul, pp. 938—941.

Byun, D.; Budiono, Yang, J. EL; Lee, C. & Lim, K. W. (2005). Numerical visualization of flow instability in microchannel considering surface wettability. *2nd International Conference on Fuzzy Systems and Knowledge Discovery,* Changsha, LNAI 3613, pp. 1113-1116.

Chen, X.; Lam, Y. C.; Chen, X. Y.; Chai, J. C. & Yang, C. (2006). Numerical simulation of electroosmotic flow with step change in zeta potential. https://dspace.mit .edu/bitstream/1721. 1/7457/1/IMST018.pdf, accessed on 21-08-2006.

Dalton, T.; Eason, C.; Enright, R.; Hodes, M.; Kolodner, P. & Krupenkin, T. (2006). Challenges in using nano textured surfaces to reduce pressure drop through microchannels. *7th International Conference on Thermal, Mechanical and Multiphysics Simulation and Experiments in Micro-Electronics and Micro-Systems,* Milano, pp. 1—3.

Dargush, G. & Banerjee, P. (1990). Development of an integrated bem for hot fluid-structure interaction. *Journal of Engineering for Gas Turbines and Power-Transactions of the ASME,* 112-2, pp. 243-250.

Deval, J.; Umali, T. A.; Lan, E. H.; Dunn, B. & Ho, C. M. (2004). Reconfigurable hydrophobic/hydrophilic surfaces in microelectromechanical systems (MEMS). *J. Micromech. Microeng*., 14, pp. 91–95.

Erickson, D. (2005). Towards numerical prototyping of labs-on-chip: modeling for integrated microfluidic devices. *Microfluidics and Nanofluidics,* 1, pp. 301-318. 19

CFD-ACE+ V2006 software manuals. ESI CFD Inc., 2006.

CFD-ACE+ V2007.2 software manuals. ESI CFD Inc., 2007.

Fan, D. & Tijsseling, A. (1992). Fluid structure interaction with cavitation in transient pipe flows. *Journal of Fluids Engineering-Transactions of the ASMS,* 114-2, pp. 268-274.

Fu, L. M.; Lin, J. Y. & Yang, R. J. (2003). Analysis of electroosmotic flow with step change in zeta potential. *Journal of Colloid and Interface Science,* 258, pp. 266-275.

Fujita, K. (1990). Flow-induced vibration and fluid structure interaction in nuclear power plant components. *Journal of Wind Engineering and Industrial Aerodynamics,* 33-1-2, pp. 405-418.

Herr, A. E.; Molho, J. I.; Santiago, J. G.; Mungal, M. G. & Kenny, T. W. (2000). Electroosmotic capillary flow with nonuniform zeta potential. *Analytical Chemistry*, 72, pp. 1053–1057.

Hirt, C. W. & Nichols, B. D. (1981). Volume of fluid (VOF) method for the dynamics of free boundaries. *Journal of Computational Physics,* 39, pp. 201-225.

Huang, W.; Liu, Q. & Li, Y. (2006). Capillary filling flows inside patterned-surface microchannels. *Chem. Eng. Technol,* 26, pp. 716-723.

Karimi, G. & Li, X. (2005). Electroosmotic flow through polymer electrolyte membranes in PEM fuel cells. *Journal of Power Sources*, 140, pp. 1–11.

Kim, D. S.; Lee, K. C.; Kwon, T. H. & Lee, S. S. (2002). Microchannel filling flow considering surface tension effect. *J. Micromech. Microeng*. 12, pp. 236–246.

Kock, E. & Olson, L. (1991). Fluid structure interaction analysis by the finite element method - a variational approach. *International Journal for Numerical Methods in Engineering,* 31-3, pp. 463—491.

Kothe, D. B.; Rider, W. J.; Mosso, S. J. & Brock, J. S. (1996). Volume tracking of interfaces having surface tension in two and three Dimensions. *AIAA Paper,* 96-0859, pp. 1-18.

Lee, J. S. H.; Ren, C. L. & Li, D. (2005). Effects of surface heterogeneity on flow circulation in electroosmotic flow in microchannels. *Analytica Chimica Acta,* 530, pp. 273-282.

Li, S.; Lowengrub, J. S. & Leo, P. H. (2007). A rescaling scheme with application to the long-time simulation of viscous fingering in a Hele-Shaw cell. *Journal of Computational Physics,* 225, pp. 554-567.

Liechty, B.; Webb, B. W. & Maynes, R. D. (2005). Convective heat transfer characteristics of electro-osmotically generated flow in microtubes at high wall potential. *International Journal of Heat and Mass Transfer,* 48, pp. 2360-2371.

Lui, A. & Lou, J. (1990). Dynamic coupling of a liquid-tank system under transient excitations. *Journal of Ocean Engineering,* 17-3, pp. 263-277.

Mitra, S. K. & Saha, A. A. (2008). Methods for surface modification. Encyclopedia of Microfluidics and Nanofluidics, *Springer- Verlag Heidelberg,* Germany.

Madou, M. (2002). Fundamentals of Microfabrication. *CRC Press,* New York.

Moondra, S.; Upadhyay, A. & Mitra, S. K. (2006). Investigation of fluid structure interaction of an elastic membrane in a microchannel. http://comsol.cntech.com.cn/conf2006/papers/Fluid-Structure_Interactions/Mitra/Mitra.pdf, accessed on 29-12-2007.

Nayak, K.; Kulkarni, P. D.; Deepu, A.; Sitaraman, V. R.; Punidha, S.; Saha, A. A.; Ravikanth, M.; Mitra, S. K.; Mukherji, S. & Rao, V. R. (2007). Patterned microfluidic channels using self-assembled hydroxy-phenyl porphyrin monolayer. *7th IEEE International Conference on Nanotechnology,* Hong Kong, Paper No. 404, pp. 1-5.

Olson, L. & Bathe, K. (1985). An infinite element for analysis of transient fluid-structure interaction. *Journal of Engineering with Computers,* 2, pp. 319-329.

Patankar, S. (1980). Numerical Heat Transfer and Fluid Flow. *Hemisphere Publishing Corp.,* New York.

Pinsky, P. & Abboud, N. (1989). Two mixed variational principles for exterior fluid structure interaction problems. *Journal of Computers and Structures,* 33-3, pp. 621—635.

Probstein, R. (1994). Physicochemical Hydrodynamics. *Wiley* , New York.

Raessi, M.; Mostaghimi, J. & Bussmann, M. (2007). Advecting normal vectors: A new method for calculating interface normals and curvatures when modeling two phase flows. *Journal of Computational Physics,* 226, pp. 774-797.

Rawool, A. S.; Mitra, S. K. & Kandlikar, S. G. (2006). Numerical simulation of flow through microchannels with designed roughness. *Microfluidics and Nanofluidics,* 2, pp. 215-221.

Rawool, A. S. & Mitra, S. K. (2006). Numerical simulation of electroosmotic effect in serpentine channels. *Microfluidics and Nanofluidics,* 2, pp. 261-269.

Saha, A. A.; Mitra, S. K. & Li, X. (2007). Electroosmotic effect on flows in a serpentine microchannel with varying zeta potential. *Journal of Power Sources,* 164, pp. 985-991.

Saha, A. A. & Mitra, S. K. (2007). Investigation of three-dimensional flow in microchannels with patterned surfaces. *5th International Conference on Nanochannels, Microchannels and Minichannels,* Puebla, Mexico, Paper No. 30052, pp. 1-8.

Saha, A. A. & Mitra, S. K. (2008). Investigation of capillary flow in microchannels with alternate hydrophilic-hydrophobic bottom wall. *Langmuir,* under review.

Salamon, T.; Lee, W.; Krupenkin, M.; Hodes, M. & Kolodner, P. (2005). Numerical simulation of fluid flow in microchannels with superhydrophobic walls. *International Mechanical Engineering Conference and Exposition,* Orlando, Florida, Paper No. 82641, pp. 1-11.

Seybert, A. F.; Wu, T. & Li, W. (1993). A coupled FEM/BEM for fluid-structure interaction using ritz vectors and eigenvectors. *Journal of Vibration and Acoustics-Transactions of the ASME,* 115-2, pp. 152-158.

Souders, D.; Khan, I.; Yao, G. F.; Incognito, A. & Corrado, M. (2003). A numerical model for simulation of combined electroosmotic and pressure driven flow in microdevices. *7th International Symposium on Fluid Control, Measurement and Visualization,* Perronte, pp. 1—7.

Stange, M.; Dreyer, M. E. & Rath, H. J. (2003). Capillary driven flow in circular cylindrical tubes. *Physics of Fluids,* 15, pp. 2587-2601.

Sujatha, K. S.; Matallah, H.; Banaai, M. J. & Webster, M. F. (2006). Computational predictions for viscoelastic filament stretching flows: ALE methods and free-surface techniques (CM and VOF). *Journal of Non-Newtonian Fluid Mechanics,* 1137, pp. 81-102.

Trutschel, R. & Schellenberger, U. (1998). Dynamic simulation of free surfaces in capillaries with the finite element method. *International Journal for Numerical Methods in Fluids,* 26, pp. 485-495.

Vonestorff, O. & Antes, H. (1991). On FEM-BEM coupling for fluid structure interaction analyses in the time domain. *International Journal for Numerical Methods in Engineering,* 31-6, pp. 1151—1168.

Washburn, E. W. (1921). The dynamics of capillary flow. *Phys. Rev.,* 17, pp. 273-299.

Wilson, E. & Khalvati, M. (1983). Finite elements for the dynamic analysis of fluid-solid systems. *International Journal of Numerical Methods in Engineering,* 19, pp. 1657—1668.

Yang, L. J.; Yao, T. J. & Tai, Y. C. (2004). The marching velocity of the capillary meniscus in a microchannel. *J. Micromech. Microeng.,* 14, pp. 220-225.

Yang, H. Q. & Przekwas, A. J. (1998). Computational modeling of microfluid devices with free surface liquid handling. *1st International Conference on Modeling and Simulation of Microsystems,* San Juan, Puerto Rico, pp. 498-505.

Yian, D. & Lawal, A. (2006). Numerical study on gas and liquid slugs for Taylor flow in a T-junction microchannel. *Chemical Engineering Science,* 61, pp. 7609-7625.

Zeng, J. (2007). On modeling of capillary filling. http://www.coventor.com/pdfs/on modeling of capillary filling.pdf, accessed on 15-03-2007.

Zeng, X. J. B. & MacCamy, R. (1992). Stable variational coupling method for fluid-structure interaction in semi-infinite media. *Journal of Vibration and Acoustics-Transactions of the ASME,* 114-3, pp. 387—396.

Zhang, J.; He, G. & Liu, F. (2006). Electroosmotic flow and mixing in heterogeneous microchannels. *Physical Review E,* 73, 050301.

Zhao, B.; Jeffrey, M. S. & Beebe, D. J. (2001). Surface-directed liquid flow inside microchannels. *Science,* 291, pp. 1023-1026.

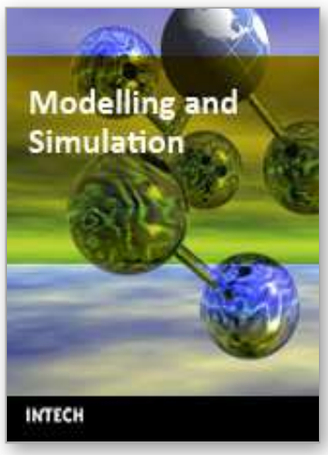

Modelling and Simulation

Edited by Giuseppe Petrone and Giuliano Cammarata

ISBN 978-3-902613-25-7
Hard cover, 688 pages
Publisher I-Tech Education and Publishing
Published online 01, June, 2008
Published in print edition June, 2008

This book collects original and innovative research studies concerning modeling and simulation of physical systems in a very wide range of applications, encompassing micro-electro-mechanical systems, measurement instrumentations, catalytic reactors, biomechanical applications, biological and chemical sensors, magnetosensitive materials, silicon photonic devices, electronic devices, optical fibers, electro-microfluidic systems, composite materials, fuel cells, indoor air-conditioning systems, active magnetic levitation systems and more. Some of the most recent numerical techniques, as well as some of the software among the most accurate and sophisticated in treating complex systems, are applied in order to exhaustively contribute in knowledge advances.

InTech Europe
University Campus STeP Ri
Slavka Krautzeka 83/A
51000 Rijeka, Croatia
Phone: +385 (51) 770 447
Fax: +385 (51) 686 166
www.intechopen.com

InTech China
Unit 405, Office Block, Hotel Equatorial Shanghai
No.65, Yan An Road (West), Shanghai, 200040, China
中国上海市延安西路65号上海国际贵都大饭店办公楼405单元
Phone: +86-21-62489820
Fax: +86-21-62489821

IntechOpen